Isopycnal Eddy Diffusivities and Critical Layers in the Kuroshio Extension from an Eddying Ocean Model

RU CHEN, JULIE L. MCCLEAN, AND SARAH T. GILLE

Scripps Institution of Oceanography, University of California, San Diego, La Jolla, California

ALEXA GRIESEL

KlimaCampus, University of Hamburg, Germany

(Manuscript received 27 November 2013, in final form 22 April 2014)

ABSTRACT

High spatial resolution isopycnal diffusivities are estimated in the Kuroshio Extension (KE) region (28°–40°N, 120°–190°E) from a global 1/10° Parallel Ocean Program (POP) simulation. The numerical float tracks are binned using a clustering approach. The number of tracks in each bin is thus roughly the same leading to diffusivity estimates that converge better than those in bins defined by a regular geographic grid. Cross-stream diffusivities are elevated in the southern recirculation gyre region, near topographic obstacles and downstream in the KE jet, where the flow has weakened. Along-stream diffusivities, which are much larger than cross-stream diffusivities, correlate well with the magnitudes of eddy velocity. The KE jet suppresses cross-stream mixing only in some longitude ranges. This study estimates the critical layer depth both from linear local baroclinic instability analysis and from eddy phase speeds in the POP model using the Radon transform. The latter is a better predictor of large mixing length in the cross-stream direction. Critical layer theory is most applicable in the intense jet regions away from topography.

1. Introduction

Mesoscale eddies dominate the global ocean kinetic energy budget (Ferrari and Wunsch 2009). They also transport and mix properties throughout the World Ocean and interact with the mean flow field, consequently playing an important role in ocean circulation and climate variability. Intense mesoscale variability is associated with western boundary currents (WBCs) once they separate from the continental shelf and flow eastward. The Kuroshio Extension (KE) is an example of such a current. The KE forms the eastward arm of the poleward North Pacific WBC and creates a front between warm, salty subtropical water to the south and cold, fresh subpolar water to the north (e.g., Donohue et al. 2008; Howe et al. 2009). Mixing of properties between these gyres arises from cross-frontal fluxes caused by eddies in the form of rings, meander crests and troughs, and frontal waves (e.g., Donohue et al. 2008; Howe et al. 2009). Significant eddy generation occurs along the front through instability processes (e.g., Kouketsu and Yasuda 2008; Waterman et al. 2011) and through jet/eddy–topography interaction. In addition, remotely generated eddies propagate into the KE system and interact with the KE front (e.g., Greene et al. 2009; Tracey et al. 2012).

The KE system consists of quasi-permanent recirculation gyres to the north and south of the jet (e.g., Jayne et al. 2009). Eddies here, as well as in the jet core, alter the mean state through eddy-mean flow interactions (e.g., Waterman et al. 2011). Eddies and the dynamic state of the KE (i.e., whether it is weakly or strongly meandering) influence the formation rates of North Pacific Subtropical Mode Water in the southern recirculation gyre (e.g., Talley et al. 1995; Qiu et al. 2007; Donohue et al. 2008; Oka and Qiu 2012). Since this water mass is coupled to air–sea heat and gas exchange, knowing the nature and spatial variability of eddy mixing in the KE region is key to gaining an improved understanding of the regional circulation and climate variability.

Corresponding author address: Ru Chen, Scripps Institution of Oceanography, University of California, San Diego, 8622 Kennel Way, La Jolla, CA 92037.
E-mail: ruchen@alum.mit.edu

DOI: 10.1175/JPO-D-13-0258.1

One of the goals of the observational Kuroshio Extension System Study (KESS) field campaign was to study the generation of mesoscale eddies and their role in cross-frontal fluid exchange in the KE region (Donohue et al. 2008). The main in situ instrument array was located to the east of Japan, centered on the first quasi-stationary meander crest and trough in the KE jet and configured to measure mesoscale variability (Donohue et al. 2008). From the KESS observations, Waterman et al. (2011) described the structure of the mean KE jet and local eddy variability, as well as the nature of eddy-mean flow interactions. Tracey et al. (2012) documented downstream propagation of KE meanders, as well as coupling between the KE jet and upstream-propagating deep-ocean eddies; the vertical coupling between these topographically controlled deep eddies was also explored by Greene et al. (2009, 2012). Bishop et al. (2013) identified upgradient eddy heat fluxes from the array, and the impact of eddies on water mass variability was reported by Qiu et al. (2007) and Qiu and Chen (2011). However, KESS encompassed too small a geographic region to allow us to study the spatial variability of diffusivity in both the along-jet and cross-jet directions. Using a pseudotrack clustering approach (Koszalka and LaCasce 2010), this study estimates the spatial distribution of eddy diffusivities in the KE region (28°–40°N, 120°–190°E) using floats that were deployed and advected online in a global eddying ocean model.

Relatively less attention has been paid to eddy mixing in the KE than in the Gulf Stream and Southern Ocean (e.g., Owens 1984; Bower and Rossby 1989; Marshall et al. 2006; Shuckburgh et al. 2009; Griesel et al. 2010; Ferrari and Nikurashin 2010; Klocker et al. 2012a). Like the Gulf Stream Extension, the KE is primarily a free inertial jet (Waterman and Jayne 2011), whereas the Antarctica Circumpolar Current (ACC) is primarily driven by momentum input by wind stress, which corresponds to about 70% of the global wind power input (Wunsch 1998). Eddy-mean flow interactions in the western boundary jets also differ from those in the ACC (Chen 2013; Chen et al. 2014). Yet, all these current systems are characterized by narrow and intense jets that are associated with a highly variable eddy field, and they all play key roles in regulating the climate system.

The vertical structure of isopycnal eddy mixing rates in the cross-mean flow (i.e., cross stream) direction in the Gulf Stream and Southern Ocean has received much attention (e.g., Bower et al. 1985; Bower and Rossby 1989; Yuan et al. 2004; Abernathey et al. 2013). Elevated cross-stream mixing occurs at middepth in the core of ACC jets (e.g., Abernathey et al. 2010; Klocker et al. 2012b); similar mixing occurs in the Gulf Stream (e.g., Owens 1984; Bower et al. 1985; Bower and Rossby 1989). Using linear baroclinic instability analysis, Lozier and Bercovici (1992) and Smith and Marshall (2009) found that elevated cross-stream mixing occurs at the critical layer depth (CLD), where the wave phase speed matches the mean flow. For a review of CLD theory, see Naveira Garabato et al. (2011). However, these studies do not capture the full range of conditions in the Southern Ocean and Gulf Stream. Klocker and Abernathey (2013) found that meridional diffusivities from satellite-derived velocities in the eastern Pacific resemble those from the diffusivity theory in Ferrari and Nikurashin (2010), which builds on the critical layer theory of Green (1970).

For the KE region, however, the vertical structures of eddy mixing rates have not been investigated, and it is unknown whether critical layer theory applies there. The goals of this study are to analyze the three-dimensional spatial structures of isopycnal eddy diffusivities at high resolution and to assess the relevance of critical layer theory to the vertical structures of mixing in the KE region. Considering that the local baroclinic instability hypothesis breaks down in the KE region (e.g., Waterman et al. 2011; Waterman and Jayne 2011; Chen 2013; Chen et al. 2014), we estimate CLD using both the local baroclinic instability analysis approach from Smith and Marshall (2009) and a new method using realistic eddy phase speeds from a global eddying ocean model. We also examine whether the mixing length theory in Ferrari and Nikurashin (2010) applies to our study domain by comparing mixing length from theory and that from numerical floats. Our results will be contrasted with the Southern Ocean findings from previous studies.

The simulated ocean circulation in standard resolution climate models is sensitive to the choice of eddy mixing parameterization (e.g., Danabasoglu and Marshall 2007), which is typically a downgradient closure scheme (e.g., Redi 1982; Gent and McWilliams 1990; Visbeck et al. 1997; Roberts and Marshall 2000). Eddy tracer fluxes with or without rotational components (Marshall and Shutts 1981) can be upgradient in western boundary current extension regions (e.g., Eden et al. 2007; Waterman and Jayne 2011; Waterman and Hoskins 2013; Bishop et al. 2013); hence, these key eddy processes may be misrepresented in coarse-resolution models. Characterizing isopycnal eddy mixing in the KE region is therefore an important step toward improving eddy parameterization schemes.

The paper is organized as follows: Section 2 describes the configuration of the global eddying model with numerical floats deployed and advected. Section 3 introduces the pseudotrack clustering approach to estimate eddy diffusivities from floats. Section 4

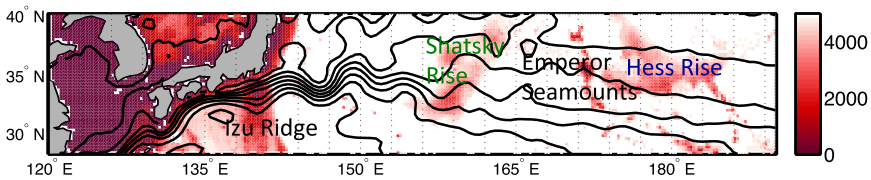

FIG. 1. Color shows the bathymetry (m) in the study domain, and black contours are streamlines averaged over the years 1994 and 1995. Streamlines are defined in Eq. (1). Blue texts denote major topographic features in this region: Izu Ridge, Shatsky Rise, Emperor Seamounts, and Hess Rise.

describes the horizontal structures of eddy diffusivities. The vertical structures of eddy mixing, CLD estimation, and the applicability of critical layer theory are discussed in section 5. Section 6 contains the summary and discussion.

2. Eddying model configuration and numerical floats

a. Model description

The Parallel Ocean Program (POP; Dukowicz and Smith 1994) model setup used in this study is that of Maltrud et al. (2010), except for the type of atmospheric forcing. It has a nominal longitudinal resolution of $1/10°$ and has 42 vertical levels with thicknesses smoothly varying from 10 m at the surface to 250 m in the lower water column, with the maximum depth occurring at 6000 m. Partial bottom cells (Pacanowski and Gnanadesikan 1998) were included to improve the representation of flows over topography and of topographic waves.

Subgrid-scale horizontal mixing was parameterized using biharmonic diffusion operators; the viscosity and diffusivity values vary spatially with the cube of the average grid cell length (see Maltrud et al. 1998). Their equatorial values, denoted by the subscript 0, are $\nu_0 = -2.7 \times 10^{10}\,\mathrm{m^4\,s^{-1}}$ and $\kappa_0 = -0.3 \times 10^{10}\,\mathrm{m^4\,s^{-1}}$, respectively. Subgrid-scale vertical mixing was parameterized using the K-profile parameterization (Large et al. 1994). No sea ice model was explicitly included; however, surface potential temperature and salinity (5 m) were tightly restored to climatological-mean observational values in regions where sea ice occurs, as identified from monthly climatological sea ice observations.

Our initial state was obtained from year 30 of the Maltrud et al. (2010) POP simulation that was forced with climatological monthly averaged "normal year" Coordinated Ocean–Ice Reference Experiments (CORE) atmospheric fluxes (Large and Yeager 2009). We ran forward from this initial state using daily CORE2 interannually varying fluxes for the years 1990–2007. Years 1990–93 were considered an adjustment period to the synoptic, interannually varying fluxes.

b. Float deployments and trajectories

One million Lagrangian floats were released online into the global domain using spacings of 0.25° in latitude and 2.5° in longitude with 23 vertical levels. The small meridional spacing is used to resolve mixing across the narrow quasi-zonal jets, whereas coarser zonal spacing is chosen as floats are rapidly advected by zonal flows. The vertical spacing below the mixed layer matches the vertical spacing of the POP model, since we do not expect to extract additional information by increasing the vertical resolution beyond the model discretization.

The numerical floats were deployed at the beginning of the year 1994 and were then advected through the three-dimensional flow for 1 yr using a fourth-order Runge–Kutta scheme (Griesel et al. 2014). The float positions as well as temperature, salinity, potential density, and velocity at these locations are saved at daily intervals. The number of floats was chosen as a trade-off between model efficiency and the need to maximize the number of trajectories in the global domain for subsequent Lagrangian statistical analysis.

The bathymetry of the KE region is shown in Fig. 1; superimposed on it are streamlines that are obtained from

$$\psi_g = gf^{-1}\eta, \tag{1}$$

where η is the time-mean sea surface height during 1994/95 from the POP model. The Izu–Ogasawara (Izu) Ridge runs perpendicular to the upstream KE flow, the Shatsky Rise is located around 160°E where the streamlines start to diverge, and the Emperor Seamounts and Hess Rise are situated farther to the east where the streamlines have significantly diverged.

Figure 2 shows eddy velocity magnitudes from the floats and the number of days that numerical floats spend in each 0.5° bin (float days) at representative

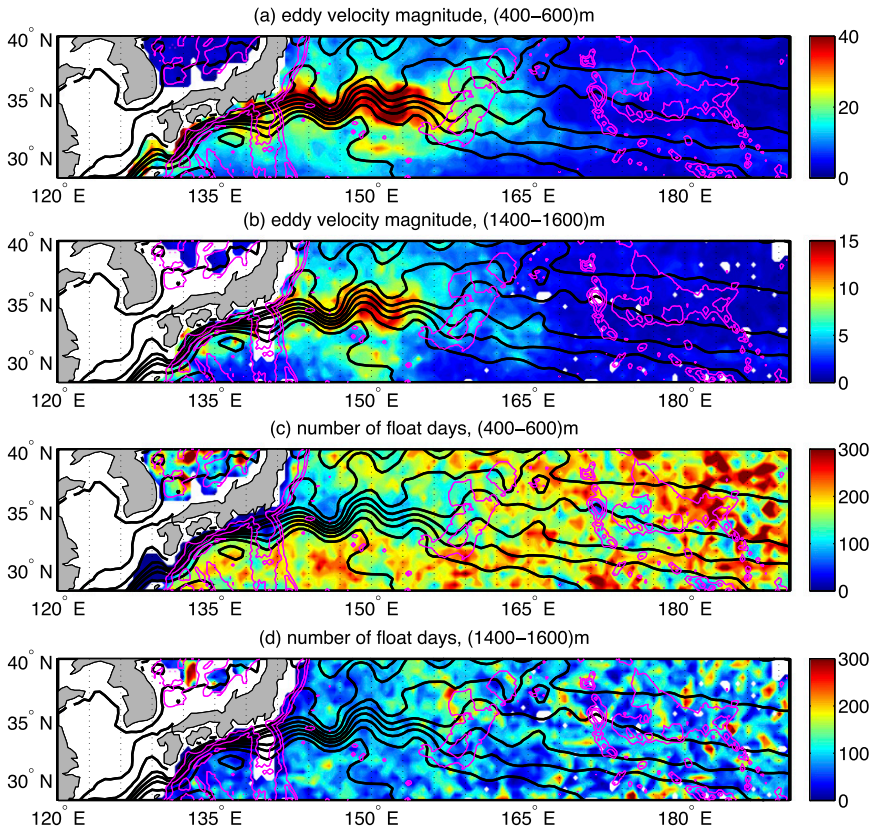

FIG. 2. Eddy velocity magnitude ($\sqrt{u'^2 + v'^2}$; cm s^{-1}) derived from float output in 0.5° geographic bins for (a) 400–600 and (b) 1400–1600 m. Number of days that the numerical floats spend in each 0.5° bins for (c) 400–600 m and (d) 1400–1600 m. Black lines denote the streamlines and magenta contours denote the 1500-, 3000-, and 4500-m bathymetry contours. The terms u' and v' were obtained by subtracting the 1994 mean Eulerian velocities from the instantaneous Eulerian velocities at the float positions.

depth intervals. Eddy velocity magnitudes for 400–600 (Fig. 2a) and 1400–1600 m (Fig. 2b) were found to be representative of those above and below 900 m, respectively; eddy velocity magnitudes in the upper 900 m are the largest in the meandering jet core between 130° and 160°E, while below 900 m, the largest magnitudes occur in the jet core at around 150°E. More float days are found in the upper ocean because of the finer vertical resolution of the float deployment there. Though the floats are deployed uniformly in the horizontal plane at the beginning of 1994, the number of float days in each regular geographic bin is spatially inhomogeneous due to the flow inhomogeneity. For the upper depth range, floats are more concentrated in patches to the east of 160°E and to the south of the jet. In the lower depth range, the highest values are seen sporadically in the western domain. In all, this leads to diffusivity estimates with convergence properties that are highly nonuniform in regular geographic bins (Koszalka and LaCasce 2010; Koszalka et al. 2011).

The variable $A_n(t)$ measures the degree to which floats move along isopycnal surfaces,

$$A_n(t) = \left\{ \frac{\partial \overline{\rho}}{\partial z}[\mathbf{x}_n(t)] \right\}^{-1} \frac{d\rho_n(t)}{dt}, \tag{2}$$

where $\rho_n(t)$ is the potential density of the nth float at time t with surface as the reference level, $\overline{\rho}$ is the 2-yr (1994/95) mean potential density, and $\mathbf{x}_n(t)$ is the position of the nth float at time t. For 92% of the floats, over the 1-yr period, the time mean of $A_n(t)$ is less than 0.2 m day^{-1}. This indicates that the daily mean distance that most floats drift away from isopycnals is small. The standard deviation of $A_n(t)$ for 98% of the floats is less than 3 m day^{-1}, indicating that most floats fluctuate relative to a mean isopycnal surface by less than 3 m day^{-1}. Given the small time mean and standard deviation of $A_n(t)$, following Griesel et al. (2014), we assume that the diffusivity inferred from the horizontal

motions of these floats represents isopycnal diffusivity, not diapycnal diffusivity.

3. Methodology to diagnose isopycnal eddy diffusivities

a. Choice of diffusivity formulation

Critical layer theory predicts a local maximum of cross-jet eddy mixing at the critical layer depth due to a reduced suppression factor (e.g., Ferrari and Nikurashin 2010); mixing suppression occurs when eddies propagate relative to the mean flow. To explore this possibility, we will examine eddy diffusivities both along and across the time-mean Eulerian velocity directions. These diffusivity components will hereafter be referred to as cross-stream ($\kappa_\perp$) and along-stream ($\kappa_\parallel$) diffusivities. To compare our results in the KE region with analogous findings in the Southern Ocean (e.g., Griesel et al. 2010, 2014), we use the diagnostic formulas employed by Griesel et al. (2010, 2014):

$$\kappa_\perp(\mathbf{x},\tau) = \int_0^\tau d\tilde{\tau}\langle u'_\perp(t_0\,|\,\mathbf{x},t_0)u'_\perp(t_0+\tilde{\tau}\,|\,\mathbf{x},t_0)\rangle_L\,, \quad (3)$$

and

$$\kappa_\parallel(\mathbf{x},\tau) = \int_0^\tau d\tilde{\tau}\langle u'_\parallel(t_0\,|\,\mathbf{x},t_0)u'_\parallel(t_0+\tilde{\tau}\,|\,\mathbf{x},t_0)\rangle_L\,, \quad (4)$$

where $\langle\cdot\rangle$ denotes the ensemble average of many floats. The time lag τ can be either positive or negative. Here $u'_\perp(t_0+\tilde{\tau}\,|\,\mathbf{x},t_0)$ denotes the residual velocity, projected in the direction perpendicular to the time-mean Eulerian flow, at time $t_0+\tilde{\tau}$, when the float passes position $\mathbf{x}$ at time t_0. Similarly, $u'_\parallel(t_0+\tilde{\tau}\,|\,\mathbf{x},t_0)$ is the residual velocity in the direction of the time-mean Eulerian flow. Residual velocities denote the float velocities subtracted from the local "time-mean" Eulerian velocity at the float position. We remove the local time mean rather than the spatially uniform time mean from the float velocities, in order to reduce the contribution of the dispersion due to the mean flow shear to the estimated diffusivities (Griesel et al. 2010). Results shown next use residual velocities from which 2-yr mean Eulerian velocities are removed; removal of 1-yr means leads to similar results.

More detailed discussion about the diffusivity formulation, including the minimization of the dispersion from mean flow shear, is provided by Griesel et al. (2010). Equations (3) and (4) are consistent with the diffusivity estimation framework by Davis (1987, 1991), which extends the Taylor (1921) diffusivity for homogeneous flow to the case with inhomogeneities and mean flow. In contrast to the approach that we employed, Rypina et al. (2012) introduced an alternative Lagrangian approach to examine the eddy-induced dispersion through constructing "spreading ellipses," which can indicate the dominant dispersion direction.

b. Choice of the bin type: Pseudotrack clustering approach

The ensemble average in the diagnostic formulas [Eqs. (3) and (4)] can be computed by averaging the autocorrelation functions over all the float tracks passing through a chosen finite area (or bin) (e.g., Griesel et al. 2010; Klocker et al. 2012b). Regular geographic bins or streamline-based bins, used in earlier studies (e.g., McClean et al. 2002; Zhurbas and Oh 2003; Griesel et al. 2010), can contain very different numbers of float trajectories. This leads to highly variable uncertainties in the diffusivity estimates. For example, in the KE region, the streamlines ψ_g squeeze together in the longitude range where the jet flow is intense and then abruptly diverge in the longitude range where the jet is weaker (Fig. 2). Some streamline bins in the upstream of the KE jet cover small areas and therefore have few float trajectories, whereas farther downstream in the KE jet, the streamline-based bins are geographically large and contain many trajectories, which results in small error bars but coarse spatial resolution.

The adaptive bin clustering method from Koszalka and LaCasce (2010) leads to diffusivity estimates that converge at high resolution. Thus, this approach can resolve both along-stream and cross-stream structures of eddy mixing, allowing us to assess how jets, eddies, and topography influence eddy mixing. We construct adaptive bins in two steps. First, the positions of the floats passing through our study domain at the selected depth range of $[h_1, h_2]$ were gathered every other day. We track each float position backward and forward for another 69 days. These 139-day float track segments are termed pseudotrajectories, following Klocker et al. (2012b). Diffusivity structures are not sensitive to the choice of segment length (i.e., 119, 139, or 199 days). Second, we used the midpositions of these pseudotrajectories and the clustering algorithm of Koszalka and LaCasce (2010) to construct irregularly distributed adaptive bins for the depth range of $[h_1, h_2]$. We apply this method for 11 nonoverlapping depth ranges. These bins have variable sizes and shapes. Each bin contains around 500 pseudotrajectories, corresponding to an average bin size of 1.4° × 1.4°. At 400–600 m, the bins outside of the KE jet are denser, since floats travel more rapidly within the KE jet, and thus fewer float days are available within the current (Fig. 3). In the deep ocean, large areas without coverage are due to slow advective time scales there.

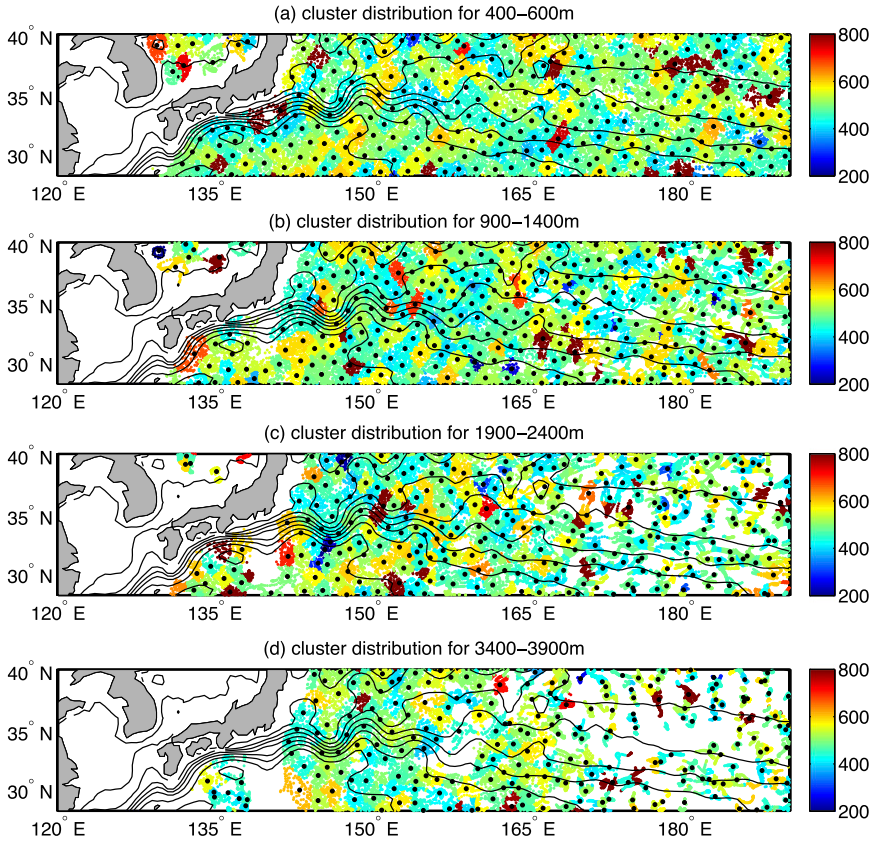

FIG. 3. Location of centroids for each adaptive bin (black dots) at four selected depth intervals: (a) 400–600, (b) 900–1400, (c) 1900–2400, and (d) 3400–3900 m. The number of pseudotracks for each bin is around 500, and the length of each pseudotrack is 139 days. Colored areas denote the coverage of the midpositions of the tracks for each bin, and the color denotes the number of tracks per bin. Black lines denote the streamlines.

Our adaptive bin construction method differs in two respects from that of Koszalka and LaCasce (2010). First, we use three dimensions rather than two. Since the number of float days decreases with depth (Fig. 2), we increase the depth interval from 125 m at the surface to 500 m in the deep ocean (Fig. 3) to keep the spatial resolution at different depth ranges roughly the same. Second, Koszalka and LaCasce (2010) broke each float trajectory into nonoverlapping segments and used the midpoints of these segments to construct their bins. In contrast, we break each float trajectory into pseudotrajectories. Pseudotrajectories from the same float trajectory can have some overlap with each other, as illustrated in the diagrams in Griesel et al. (2010) and Klocker et al. (2012b). Therefore, more pseudotrajectories are available than for the nonoverlapping segment case, and thus higher spatial resolution diffusivity estimates are obtained. Using pseudotrajectories also improves the temporal resolution: nonoverlapping segments represent only a limited number of points in time, while the overlapping segments are more effective at representing eddy mixing over the entire time period.

c. *Convergence comparison between adaptive bins and geographic bins*

Converged diffusivities in a selected bin for positive τ and negative τ are defined as

$$\kappa_{+\infty} = \frac{\int_{\tau_1}^{\tau_2} \kappa(\tilde{\tau})\, d\tilde{\tau}}{\tau_2 - \tau_1} \quad \text{and} \quad \kappa_{-\infty} = \frac{\int_{-\tau_2}^{-\tau_1} \kappa(\tilde{\tau})\, d\tilde{\tau}}{\tau_2 - \tau_1}. \tag{5}$$

Here $[\tau_1, \tau_2]$ and $[-\tau_2, -\tau_1]$ are within the lead–lag range when $\kappa(\tilde{\tau})$ has reached convergence. Our convergence criterion is presented in the appendix. In this study, $[\tau_1, \tau_2]$ and $[-\tau_2, -\tau_1]$ are respectively the first and last 20 days in each overlapping segment, as indicated by the red lines in Fig. A1. These values are chosen because most bins converge over these two ranges. Diffusivities presented in sections 4 and 5 are

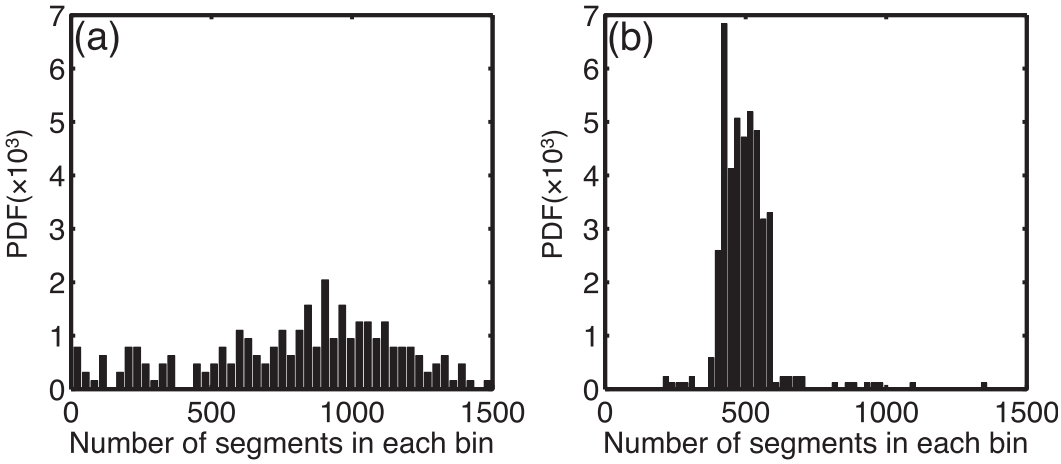

FIG. 4. Probability density function of the number of pseudotracks with midpositions passing through 2° × 2° (a) geographic bins and (b) adaptive bins located between 900 and 1400 m.

$$\kappa_{\infty} = \frac{\kappa_{+\infty} + \kappa_{-\infty}}{2}. \tag{6}$$

Consistent with Koszalka and LaCasce (2010), we find that the number of float tracks in regular bins varies much more than in adaptive bins. Probability density functions of numbers of pseudotracks with midpositions passing through 2° × 2° geographic and adaptive bins at depths between 900 and 1400 m (Fig. 4) show a broad range of values for geographic bins, while for adaptive bins, the number of pseudotracks is predominantly between 400 and 600. In Table 1, we compare convergence statistics of eddy diffusivities, as measured by the percentage of bins, for four types of bins: adaptive and geographic having resolutions of 1.4° × 1.4° and 2° × 2°. Better convergence is achieved when using adaptive bins rather than geographic bins and when using large (i.e., low resolution) bins rather than smaller (i.e., high resolution) bins. In the four cases in Table 1, the percentage of bins with symmetric convergence is the largest, and the percentage of bins with asymmetric convergence is the second largest. If we switch from adaptive bins to geographic bins at the same spatial resolution, the percentage of zero-side convergence cases increases 2 to 13 times, and the percentage of the two-side convergence cases (symmetric convergence and asymmetric convergence) decreases. For any given bin type, although the percentage of two-side convergence cases increases as we decrease the resolution, the percentage of two-side asymmetric convergence cases decreases.

d. *Choice of the bin size: Nonlocalness of the diffusivity estimates*

Our diffusivity estimates are nonlocal. Floats passing through one adaptive bin can possibly travel to adjacent bins in the time period before κ asymptotes; thus, the diffusivity estimate in each bin could be a combination resulting from mixing in several adjacent bins. In fact, all types of float-based diffusivity estimates are nonlocal (Rypina et al. 2012). To quantify the nonlocalness of our

TABLE 1. Percentage of bins for each convergence type. Adaptive denotes the adaptive bins from the clustering algorithm and geographic denotes regular geographic bins. Numbers, in degrees, in the header denote the averaged size of the adaptive bins and the size of the regular geographic bins. Residual velocities in these diffusivity calculations are the float velocity subtracted from the 2-yr (1994/95) time-mean Eulerian velocity. Length of pseudotracks for all cases are 139 days. The vertical resolution is the same in all the cases; the 11 depth ranges are described briefly in the text.

Case number, bin type, bin size	Case 1, Adaptive, 1.4°	Case 2, Adaptive, 2°	Case 3, Geographic, 1.4°	Case 4, Geographic, 2°
Symmetric converged $k_{\perp}$	44.8	65.3	39.0	54.5
Asymmetric converged $k_{\perp}$	39.5	30.3	37.9	32.9
One-side converged $k_{\perp}$	14.4	4.1	14.1	7.2
Zero-side converged $k_{\perp}$	1.3	0.4	9.0	5.5
Symmetric converged $k_{\parallel}$	45.0	62.2	38.8	56.6
Asymmetric converged $k_{\parallel}$	39.9	29.8	37.5	29.9
One-side converged $k_{\parallel}$	12.1	6.1	13.9	7.2
Zero-side converged $k_{\parallel}$	3.0	2.0	9.9	6.2

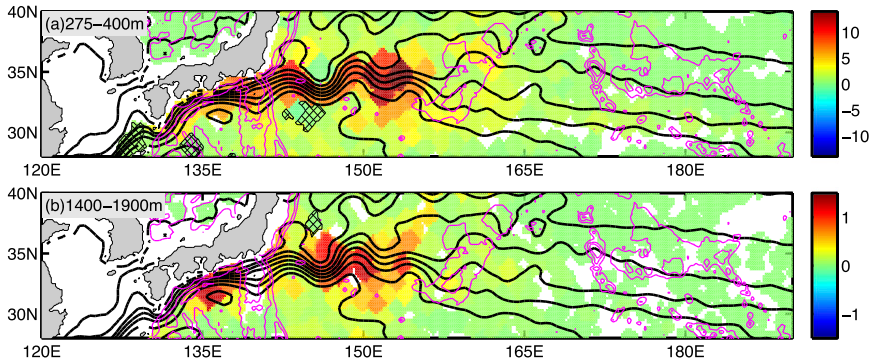

FIG. 5. Color shading represents along-stream diffusivities ($10^4\,\mathrm{m^2\,s^{-1}}$) at (a) 275–400 and (b) 1400–1900 m. These diffusivities are obtained using the methodology in section 3 and adaptive bins in Fig. 3. Diffusivities shown here are those interpolated to regular geographic bins at 0.2° resolution. Residual velocity is the deviation of float velocity from the time mean Eulerian velocity over the years 1994/95. Regions with zero-side converged or one-side converged diffusivity estimate are masked out. Black contours are those of streamlines. Magenta lines are the 1500-, 3000-, and 4500-m bathymetry contours. The hatched area indicates regions where diffusivities are statistically insignificant at the 95% confidence level (i.e., the magnitude of diffusivity is smaller than the two standard error using a bootstrap technique).

diffusivity estimates, we define the variance ellipse (e.g., Morrow et al. 1994) of positions of pseudotrajectories passing through each adaptive bin.

We define σ_1^2 as the variance of float positions along the major axis,

$$\sigma_1^2 = \frac{1}{2}\left[\sigma_x^2 + \sigma_y^2 + \sqrt{(\sigma_x^2 - \sigma_y^2)^2 + 4(\sigma_{xy}^2)^2}\right], \qquad (7)$$

and define σ_2^2 as that along the minor axis,

$$\sigma_2^2 = (\sigma_x^2 + \sigma_y^2) - \sigma_1^2. \qquad (8)$$

Here σ_x^2 represents the variance of zonal float positions relative to the centroid of each adaptive bin:

$$\sigma_x^2 = \frac{\int_{-\tau_a}^{\tau_b} \sum_{i=1}^{N} [x_i(t) - x_c(t)]^2\, dt}{[N(\tau_b + \tau_a)]}, \qquad (9)$$

where $x_i(t)$ and $y_i(t)$ are the zonal and meridional positions at time t of the ith float passing through the selected bin. The terms x_c and y_c are the zonal and meridional position of the centroid of the selected bin. Replacing $x_i(t)$ and x_c with $y_i(t)$ and y_c in Eq. (9), we obtain the variance of meridional float positions relative to the bin centroid σ_y^2. The term σ_{xy}^2 denotes the cross covariance of float positions:

$$\sigma_{xy}^2 = \frac{\int_{-\tau_a}^{\tau_b} \sum_{i=1}^{N} [x_i(t) - x_c(t)] \cdot [y_i(t) - y_c(t)]\, dt}{[N(\tau_b + \tau_a)]}. \qquad (10)$$

The area of the variance ellipse is used as a measure of the area in which pseudotrack floats travel within the selected bin:

$$A_{\mathrm{ellipse}} = \pi\sigma_1\sigma_2. \qquad (11)$$

The spatially averaged A_{ellipse} for the 139-day pseudo–float tracks passing through each bin decreases with depth, from $600^2\,\mathrm{km}^2$ at the surface level to $200^2\,\mathrm{km}^2$ in the deep ocean (not shown). The decrease of A_{ellipse} is because velocities decrease with depth and corresponding floats travel more slowly in the deep ocean. In many bins, $\kappa(\tau)$ has asymptoted to a constant before the full time lag τ. Therefore, a more accurate measure of the nonlocalness of our diffusivity estimates is to calculate the "effective A_{ellipse}," defined as A_{ellipse} for pseudo–float tracks over the time range of $[-\tau_{\mathrm{eq1}}, \tau_{\mathrm{eq2}}]$; that is, τ_a and τ_b in Eqs. (9) and (10) are chosen to be τ_{eq1} and τ_{eq2}. The terms τ_{eq1} and τ_{eq2} are defined as the earliest lead–lag days that $\kappa(\tau)$ converges, and they can be calculated by repeating the convergence test in the appendix for each τ. At all depth levels, the domain average of the effective A_{ellipse} is less than $200^2\,\mathrm{km}^2$, which is the same order of magnitude as the adaptive bin area.

4. Horizontal diffusivity structures

Along-stream eddy diffusivities in the KE region at representative depth intervals are shown in Fig. 5. We compared their patterns with those of eddy velocity magnitudes (e.g., Figs. 2a,b) and found that elevated values of along-stream diffusivities occur mostly in

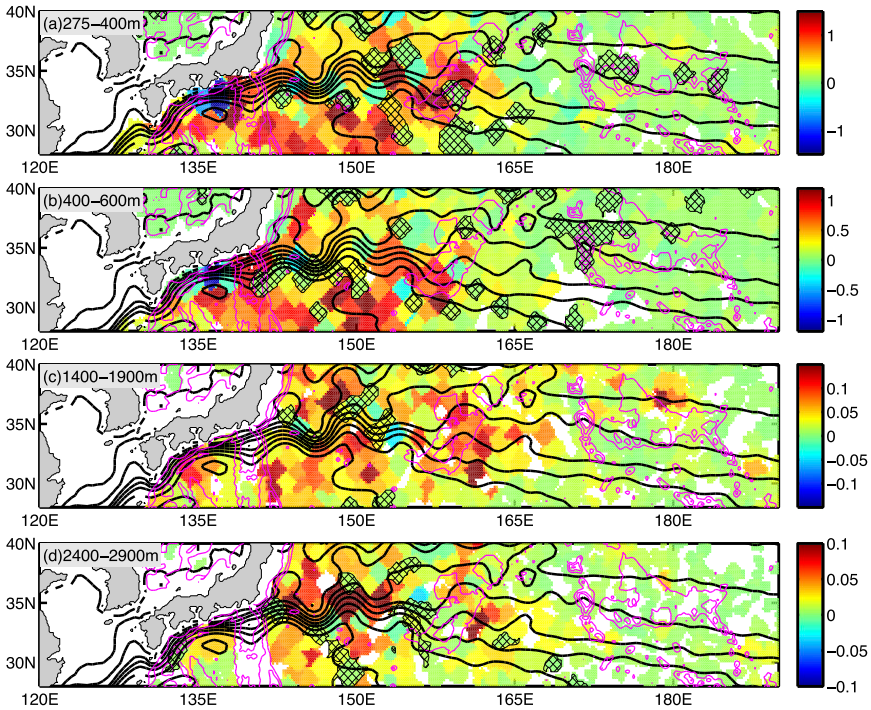

FIG. 6. As in Fig. 5, but for cross-stream diffusivities ($10^4\,m^2\,s^{-1}$) at (a) 275–400, (b) 400–600, (c) 1400–1900, and (d) 2400–2900 m.

regions characterized by high eddy velocity magnitudes, that is, to the west of 155°E in the KE jet. Along-stream diffusivities in Fig. 5a are representative of the upper 900 m: the largest values occur in the jet core extending from 130° to 155°E. Figure 5b represents depths below 900 m: again, the largest values occur in the jet core from 130° to 155°E. However, diffusivities located up to several degrees of longitude to the east of the Izu Ridge are low.

Cross-stream eddy diffusivities for four representative depth intervals are shown in Fig. 6. They have patchy structures with variations both along and across the KE jet core. These patterns are quite different from those of the along-stream eddy diffusivities. In the upper 900 m, as illustrated in Figs. 6a and 6b, elevated cross-stream mixing occurs in the jet core at the Izu Ridge where the jet leaves the coast (around 140°E), south of the jet core at 140°–150°E (i.e., the southern recirculation gyre region), and at the Shatsky Rise, where the KE jet has weakened (150°–160°E). In the middepth and deep ocean, as illustrated in Figs. 6c and 6d, cross-stream diffusivities are elevated at some topographic features. For example, cross-stream mixing is elevated east of the Izu Ridge, at and surrounding the Shatsky Rise, at some spots at the northern rim of the Hess Rise (i.e., 37°N, 180°E), in the middle part of the Emperor Seamount (i.e., 35°N, 170°E) and at the seamount chain south of the jet around 150°E. Besides these topographic features, cross-stream mixing below 1900 m is also large at the KE jet core at 145°–155°E. The magnitude of cross-stream diffusivity decreases with depth: maximum values reach around $8 \times 10^4\,m^2\,s^{-1}$ in the upper 125 m and $3500\,m^2\,s^{-1}$ at 900–1400 m; the spatially averaged values are around $5000\,m^2\,s^{-1}$ in the upper 125 m and $500\,m^2\,s^{-1}$ at around 900–1400 m.

While diffusivities are normally assumed to be downgradient and therefore positive, cross-stream diffusivities are negative at some locations. However, only 14% of negative diffusivities are statistically significant at the 95% confidence level. Regions where negative diffusivities are significant are downstream of the KE jet (145°–160°E) throughout the water column and west of the Izu Ridge (Fig. 6). Section 6 provides further discussion, but a detailed examination of the mechanisms and float behaviors responsible for these negative values is left for future study.

Diffusivity patterns here are similar to those in the Southern Ocean in the following. In both regions, differences between cross-stream diffusivity and eddy velocity patterns indicate that eddy kinetic energy alone is insufficient for parameterizing cross-stream mixing (Griesel et al. 2010; Naveira Garabato et al. 2011), in contrast with predictions from quasi-homogeneous

turbulence (Taylor 1921). In addition, the ACC acts as a barrier for cross-jet mixing only at some longitudes (Griesel et al. 2010; Naveira Garabato et al. 2011). Similarly, cross-stream mixing in the upper 900 m of the KE jet core is not suppressed at the Izu Ridge or downstream near the Shatsky Rise, but it is suppressed at 140°–155°E (Figs. 6a,b). Also, jets in the Southern Ocean are "leaky" with elevated mixing near some topographic obstacles (e.g., Griesel et al. 2010; Naveira Garabato et al. 2011; Thompson and Sallée 2012). Some mechanisms proposed to explain the leaky behavior are the large mean flow strain caused by topography (Naveira Garabato et al. 2011), unsteady jet behaviors (Thompson 2010), and the combination of eddy kinetic energy amplification and closed streamlines downstream of topography (Thompson and Sallée 2012). Enhanced cross-stream mixing at topographic obstacles also exists in our study domain (Fig. 6c); however, the relevance of these previously proposed topographic mechanisms to the KE region remains an open question. Finally, similar to the Southern Ocean (Griesel et al. 2010), along-stream diffusivities here have much larger magnitudes than those of cross-stream diffusivities. In the 11 depth intervals we selected, the ratio between the spatially averaged along-stream and cross-stream diffusivities ranges from 3 to 7 (not shown).

5. Vertical structures of mixing and application of critical layer theory

In this section, we estimate CLD (section 5a) and compare it with the depths where mixing lengths are large (section 5b). Then we compare the mixing length from critical layer theory with that from numerical floats (section 5c).

a. *Critical layer depth diagnosed from two approaches*

Both linear and weakly nonlinear wave theories, developed in an idealized fluid system with uniform mean flow and a flat bottom, predict that cross-stream mixing can have a local maximum value at the critical layer, where the wave phase speed along the mean flow direction matches the mean flow magnitude (e.g., Green 1970; Killworth 1997; Ferrari and Nikurashin 2010; Naveira Garabato et al. 2011). For example, Killworth (1997) considered the case where the mean flow can be in any arbitrary direction. He found that diffusivities are not suppressed by the mean flow when

$$\mathbf{U}\cdot\frac{\mathbf{K}}{|\mathbf{K}|}=\frac{\omega}{|\mathbf{K}|}, \tag{12}$$

which is equivalent to

$$\frac{|\mathbf{U}|k_0}{|\mathbf{K}|}=\frac{\omega}{|\mathbf{K}|}. \tag{13}$$

Here $\mathbf{U}$ is the mean flow vector, $\mathbf{K}$ is the wavenumber vector, and ω is the wave frequency. The term k_0 is the wavenumber component along the mean flow direction, and it can be obtained by projecting $\mathbf{K}$ onto the direction of $\mathbf{U}$. Therefore, a critical layer occurs when

$$|\mathbf{U}|=\omega/k_0, \tag{14}$$

that is, when the mean flow magnitude is equal to the wave phase speed along the mean flow direction. Note that ω/k_0 is positive if the wave propagates downstream and negative if it propagates upstream relative to the mean flow vector.

1) Critical layer depth from linear instability analysis

Smith and Marshall (2009) estimated CLD in the Southern Ocean using the linear local baroclinic instability analysis approach from Smith (2007). They assumed that $\mathbf{K}$ and ω in Eq. (12) are the wavenumber vector and frequency of the fastest-growing baroclinically unstable wave with the energy transfer rate of at least $5\times10^{-4}\,\mathrm{W\,m^{-2}}$ from the instability analysis. The CLD is then identified as the depth at which Eq. (12) holds for the wave with the fastest growth rate. They found that the CLD is around 1000 m in the Southern Ocean, and it is shallower on the equatorial flank of the ACC. Vollmer and Eden (2013) provided global estimates of CLD and diffusivities using the same instability analysis approach.

Using the POP time-mean geostrophic velocity and stratification fields for 1994/95, smoothed to 0.5° × 0.5° resolution using a boxcar filter, we diagnosed the CLD following Smith and Marshall (2009). Multiple solutions exist at many locations. The shallowest CLD at each grid point is shown in Fig. 7a. It is typically shallower than 500 m at the Izu Ridge and in coastal areas. The CLD in the KE jet core at 140°–155°E is more or less uniform (around 1000 m), while north and south of the jet core, the CLD has a patchy distribution of deep and shallow values. East of 160°E, the CLD is generally shallower and more uniform than it is farther west, with a spatially averaged value of 660 m. We also repeated this calculation with a more spatially smoothed 1° × 1° version of the POP fields; this showed less small-scale variability of the CLD, although the large-scale features remained the same.

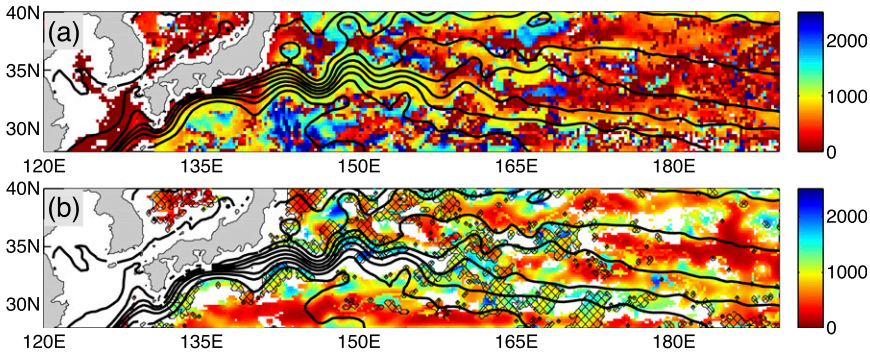

FIG. 7. The shallowest critical layer depth (m) at each location from (a) linear local baroclinic instability analysis and (b) estimated from realistic eddy phase speeds. Black contours are streamlines. The hatched area indicates the region where estimates about realistic phase speeds along-mean flow direction at the critical layer depth are unreliable, and details of estimating realistic eddy phase speeds are in Fig. 8.

2) CRITICAL LAYER DEPTH FROM THE RADON APPROACH

Southern Ocean eddies are mostly generated by baroclinic instability (e.g., Döös and Webb 1994; Drijfhout 2005; Thompson 2008); however, the linear local baroclinic instability assumption, upon which the above CLD diagnosis method is based, breaks down in the KE region. Here the eddy-mean flow interaction process is very nonlocal (Chen 2013; Chen et al. 2014); barotropic instability is as important as baroclinic instability and eddies feed energy back to the mean flow downstream of the KE jet (e.g., Qiu 1995; Hurlburt and Metzger 1998; Lebedev et al. 2003; Waterman et al. 2011; Waterman and Hoskins 2013). Thus, the wave speed here from the POP model could differ from that based on the instability analysis above.

Therefore, we estimated CLD from eddy phase speeds along the mean flow direction in the POP model, denoted by $C_{x'}$. Figure 8 illustrates how we estimate $C_{x'}$ from the Hovmöller diagram of potential vorticity (PV) anomalies using the Radon transform. Consistent with ω/k_0 in section 5a, $C_{x'}$ is positive if eddies propagate downstream and negative if they propagate upstream relative to the mean flow vector. The mean flow can be quite nonzonal in some areas; therefore, estimating phase speeds along the mean flow direction, not the zonal direction, is one key. Our $C_{x'}$ estimates are considered unreliable in areas where the mean flow varies greatly on spatial scales smaller than the length of the Hovmöller diagram (300 km here) (Fig. 8c). We obtained the CLD by comparing $C_{x'}$ in the three-dimensional spatial space with the mean flow magnitudes. The CLD from this Radon approach (Fig. 7b) does not exist in the intense KE jet from 135° to 155°E, though CLD from instability analysis (Fig. 7a) occurs there at 1000 m. East of 160°E, the CLD from the Radon approach is 820 m on average, larger than that from instability analysis by 160 m.

b. *Vertical structures of mixing and relevance of critical layer depth to elevated mixing*

Cross-stream mixing rates are influenced not only by $C_{x'} - U$, but also by eddy velocity magnitudes (Ferrari and Nikurashin 2010); therefore, to test whether critical

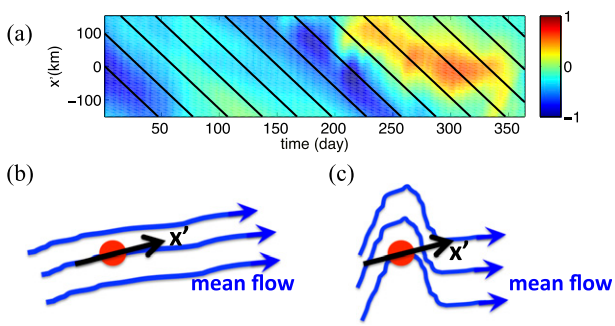

FIG. 8. (a) Hovmöller diagram of normalized PV anomalies along the x' direction extending from −150 to 150 km, at 729 m in the year 1994. Note that x' aligns with the direction of mean flow at $x' = 0$, that is, 35°N, 174°E. Eddy phase speeds along the mean flow direction, denoted by $c_{x'}$, at 35°N, 174°E can then be diagnosed from the Radon transform of the Hovmöller diagram. Black lines denote the dominant slope from Radon transform. PV anomalies denote the deviation of PV from its mean over 1994/95. In the upper 130 m, the seasonable cycle is removed from the PV anomalies before the Radon transform is carried out. (b) A schematic illustrating how to choose the direction of x' if we aim to diagnose $c_{x'}$ at the red dots. PV anomalies along the 300-km black line are extracted to form the Hovmöller diagram. (c) The case where our estimates of $c_{x'}$ do not represent eddy phase speeds along mean flow direction and thus are "unreliable." In this case, the spatial variation of the mean flow direction is large, and thus the x' direction deviates greatly from the mean flow direction at points away from the red dot. Our arbitrary criterion is that if the mean deviation along the black line is larger than 40°, our $c_{x'}$ estimate is unreliable.

layer theory applies, it is more reasonable to check whether the CLD is associated with the local maxima of cross-stream mixing length, not of cross-stream diffusivities. Cross-stream mixing length estimated from numerical floats is defined as

$$L_{\mathrm{mix}} = \frac{\kappa_{\perp}}{u_{\mathrm{rms}}\Gamma}, \tag{15}$$

where u_{rms} is the eddy velocity magnitude, that is, $\sqrt{u'^2 + v'^2}$, and Γ is a mixing efficiency (Klocker and Abernathey 2013). Generally Γ is assumed to be order one, and this study chooses $\Gamma = 0.35$, which follows Klocker and Abernathey (2013) and is consistent with Taylor (1915). The spatial structure of L_{mix} and thus the locations of large L_{mix} are independent of the choice of Γ. Results in section 5c are insensitive to Γ within the range from 0.3 to 3.

Results in the cross sections vary with longitude, and we present three representative categories based on their salient features (Figs. 9–11). A single-core jet typifies category 1 cross sections, occurring at the longitudes where the KE jet is intense and away from the main topographic features (i.e., 142°–150°E) (Fig. 9). The jet core clearly suppresses mixing in the upper 1000 m, but no local mixing maximum exists at middepth. Consistent with critical layer theory, a CLD from the Radon approach (black dots) does not exist beneath the single jet. However, the CLD from instability analysis (magenta dots) is located at around 1000 m and fails to predict the absence of a local maximum of L_{mix}. These cross sections differ from those in POP in the longitudinal ranges of the Southern Ocean where one prominent jet is found. At those longitudes, the jet acts as a cross-stream mixing barrier at the surface, but the local maximum of cross-stream mixing occurs at middepth between 1000 and 1500 m (Griesel et al. 2014). Other Southern Ocean studies also reveal these features (Abernathey et al. 2010; Cerovecki et al. 2009).

Category 2 cross sections occur east of 162°E, but away from the main topographic features in Fig. 1 (i.e., 162°–169°E) (see Fig. 10). Multiple jets exist in most of these cross sections, and these jets appear consistent with zonal jets (Maximenko et al. 2005, 2008). Here upper-ocean cross-stream mixing is suppressed by some of the jets, especially the relatively strong ones. At middepth, large mixing lengths exist in most cross sections. Most black dots (CLD from the Radon approach) and some magenta dots (CLD from instability analysis) correspond well with these middepth maxima of L_{mix}.

Category 3 cross sections occur at the main topographic features, that is, Shatsky Rise (156°–161°E), Emperor Seamount (170°–173°E), and the Hess Rise (174°–186°E). The mixing vertical structures are hard to summarize: at some cross sections, a local maximum in mixing length occurs at middepth and near the ocean bottom. But in these regions, both CLD estimates are poor predictors of large mixing length. For example, at 179°E, some jets still suppress mixing (Fig. 11c2), elevated mixing occurs near the bottom, and dots representing the CLD are not collocated with large mixing length (Fig. 11c1).

To quantitatively determine the skill of CLD in predicting local mixing maxima, we define an index, that is, the percentage of CLD points occurring at areas with elevated values of L_{mix} in each latitude–depth cross section. The elevated mixing area is defined as the region in each cross section where

$$L_{\mathrm{mix}} > \tilde{L}_{\mathrm{mix}} + \tilde{\sigma}(L_{\mathrm{mix}}). \tag{16}$$

The term $\tilde{L}_{\mathrm{mix}}$ is the median of L_{mix} in that cross section, and $\tilde{\sigma}(L_{\mathrm{mix}})$ is the standard deviation of L_{mix} relative to $\tilde{L}_{\mathrm{mix}}$. Figure 12a shows the index, which is larger far from topography (white areas) than close to topography (shaded areas). Categories 1 and 2 fall into the white area of Fig. 12a. Also, at most longitudes, the index for CLD from the Radon approach (black line) is generally larger than that for CLD from instability analysis (magenta line). In summary, the CLD from the Radon approach is a better predictor of local mixing maxima, and the CLD predicts elevated mixing better in regions away from topography (Figs. 9–12).

c. *Testing the relevance of the theoretical mixing length*

1) THEORY AND PREVIOUS WORK

Ferrari and Nikurashin (2010) employed a single-wavenumber stochastic model to extend the critical layer theory of Green (1970). They linked the cross-stream eddy mixing not only with mean flow magnitude and eddy phase speeds, but also with other eddy properties (i.e., eddy velocity magnitude, size, and decorrelation time scale). Klocker and Abernathey (2013) rewrote their diffusivity formula into a mixing length formula:

$$L_{\mathrm{mix,theory}} = \frac{L}{1 + k_{\mathrm{eddy}}^2 \gamma^{-2} (c_w - |\mathbf{U}|)^2}, \tag{17}$$

where k_{eddy} is the eddy wavenumber, γ^{-1} is the eddy decorrelation time, and $|\mathbf{U}|$ is the mean flow magnitude. The term L is considered to be the eddy length scale (Klocker and Abernathey 2013). Assuming the

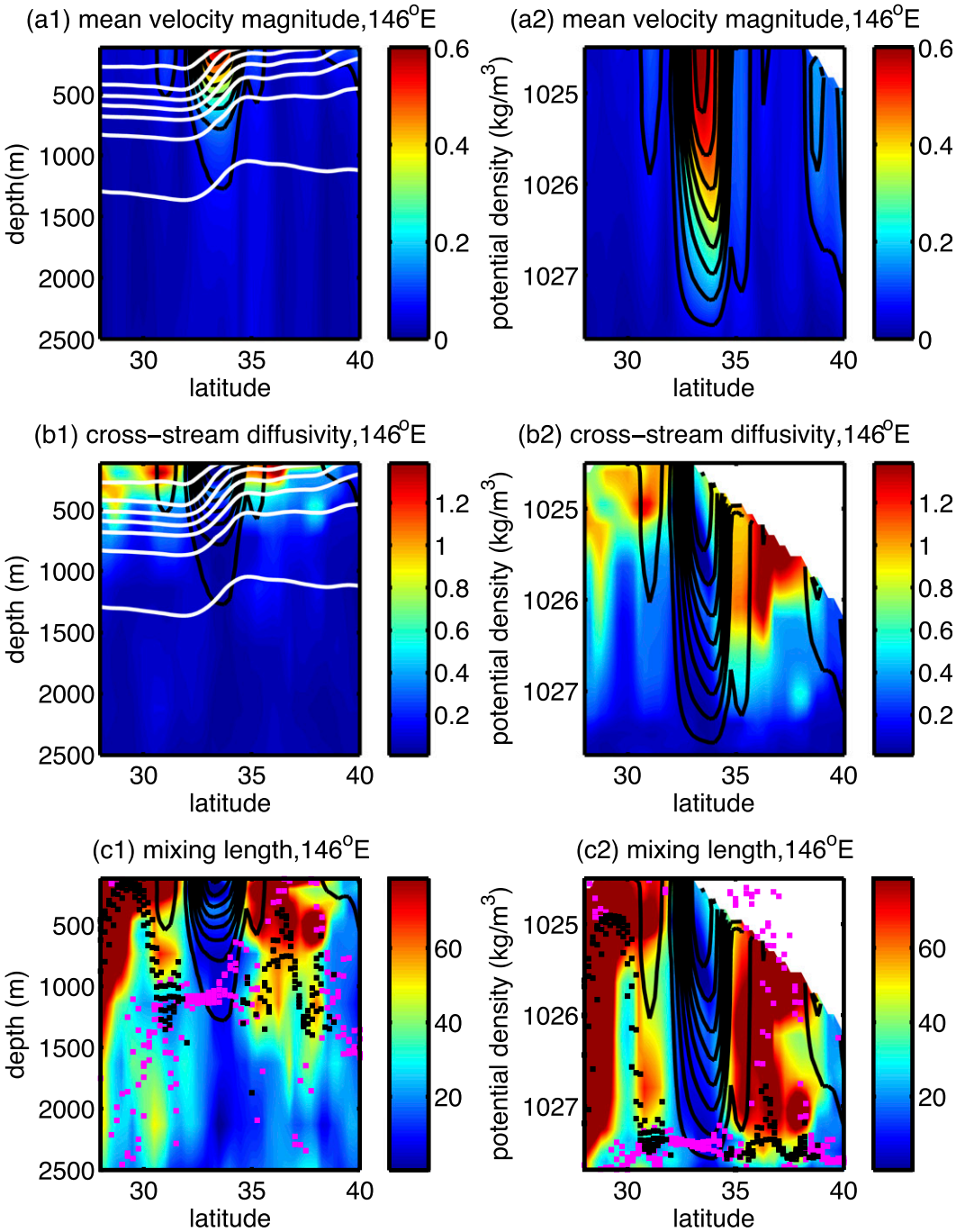

FIG. 9. Cross sections of (a1),(a2) magnitude of the time mean flow (m s^{-1}) over the years 1994/95, (b1),(b2) cross-stream diffusivities (10^4 m^2 s^{-1}), and (c1),(c2) mixing length (km) in the cross-stream direction (L_{mix}) at 146°E. Cross sections in (left) z coordinates and (right) isopycnal coordinates. Black contours are those of time mean flow magnitude, and white contours are those of the time-mean potential density over the year 1994/95. Magenta dots denote critical layer depths from Fig. 7a, and black dots are those from the nonhatched area in Fig. 7b. Adaptive bins and thus diffusivity estimates are of coarser resolution compared to that of mean velocity magnitudes from the POP model. Thus, white areas in middle and bottom panels can be larger than those in the upper panels.

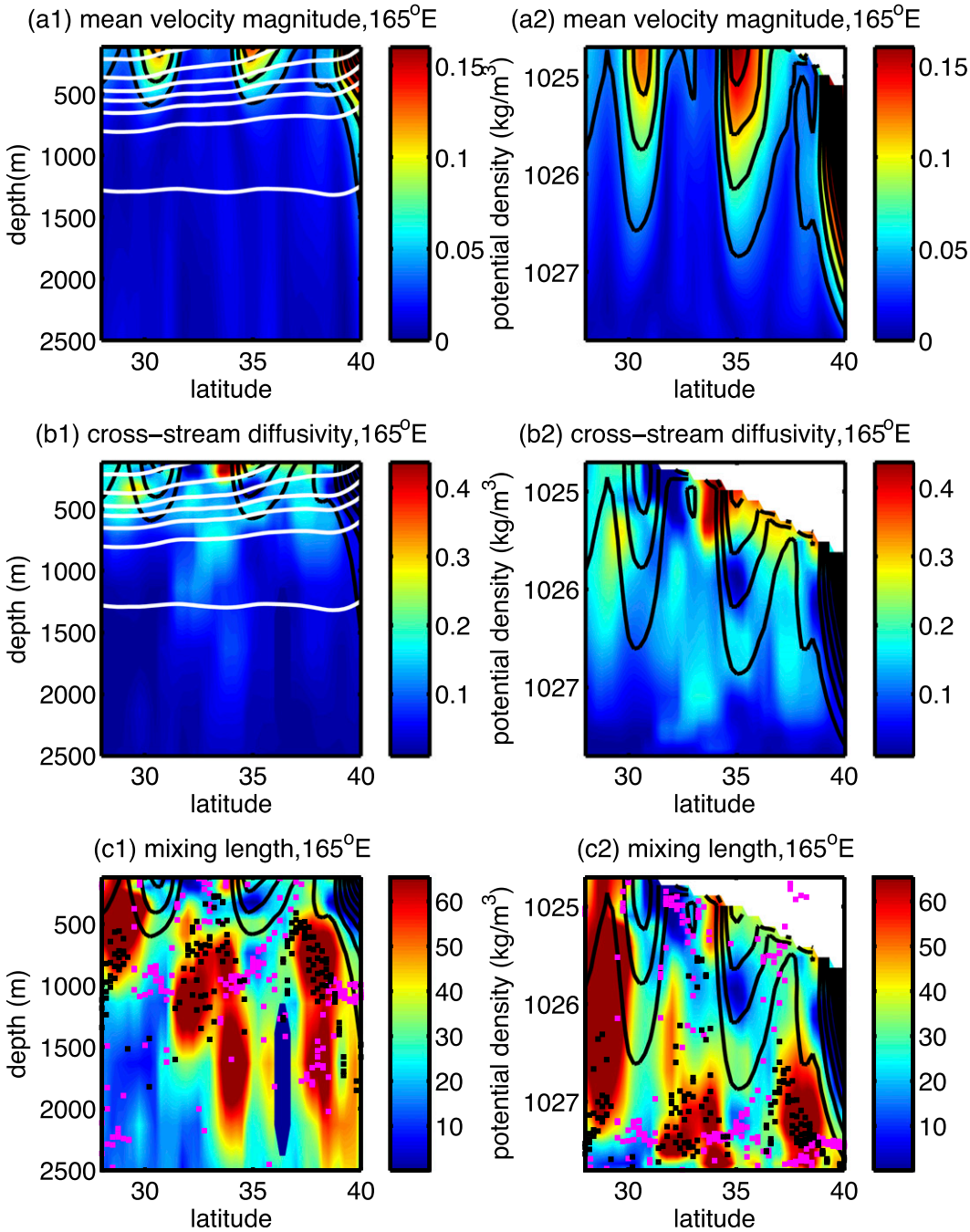

FIG. 10. As in Fig. 9, but for 165°E.

mean flow is zonal, Klocker and Abernathey (2013) and Klocker et al. (2012a) tested the relevance of the theory to the meridional or vertical structure of mixing length in the Southern Ocean and east Pacific. Note that C_w is the wave phase speed along the mean flow direction, which is not necessarily zonal. Consistent with ω/k_0 in Eq. (14), C_w is positive if the waves propagate downstream and negative if waves propagate upstream.

2) CHOICE OF EMPIRICAL EDDY PARAMETERS

One challenge to test the validity of $L_{mix,theory}$ in the ocean or models is to specify reasonable empirical eddy parameters in the mixing length formula [Eq. (17)]. The

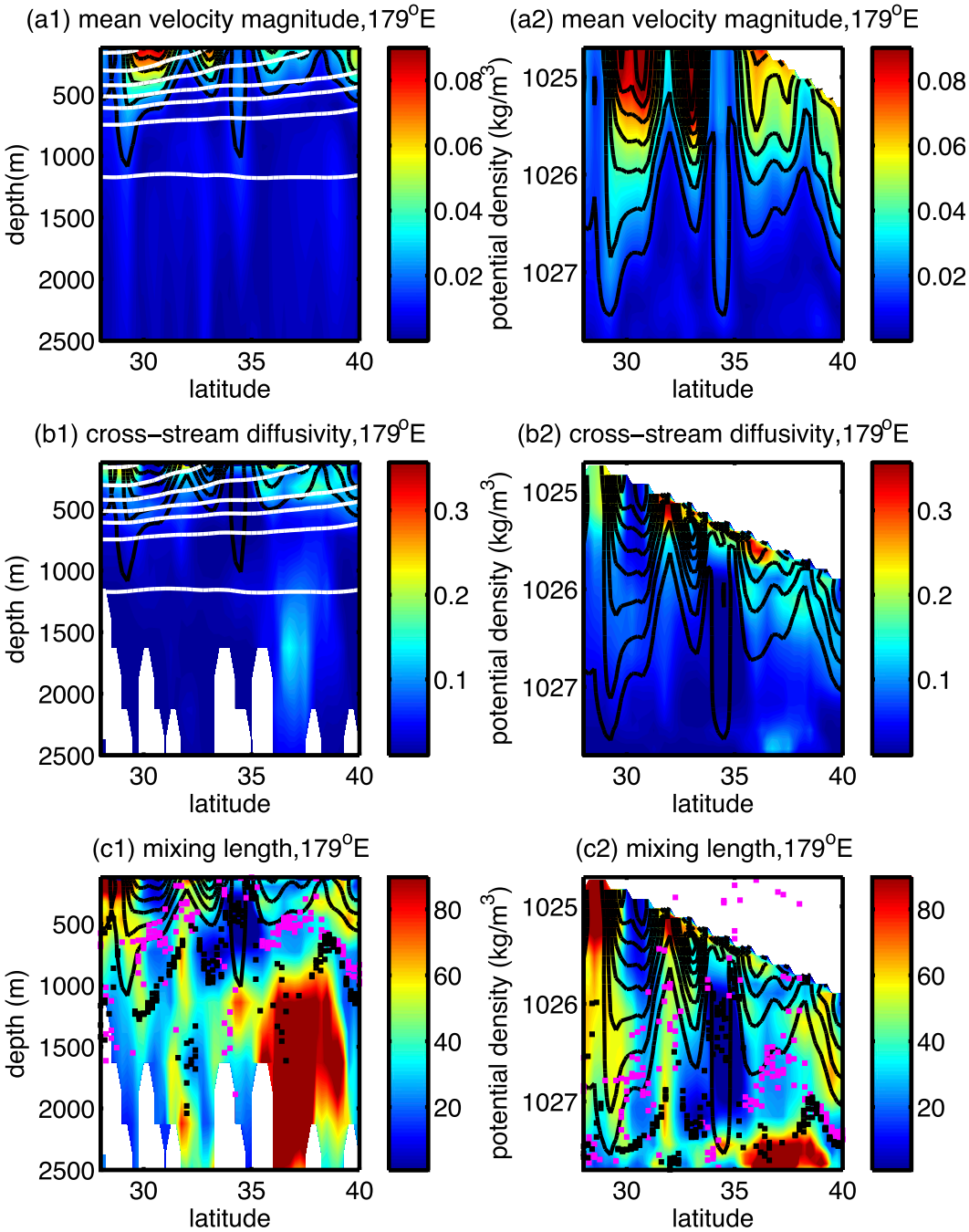

FIG. 11. As in Fig. 9, but for 179°E.

formula is based on the single-wavenumber and frequency assumption; however, the ocean eddy field includes motions with a wide range of wavenumbers, frequencies, and phase speeds (Wunsch 2010; Klocker et al. 2012a; Wortham 2013). Klocker et al. (2012a) estimated these parameters by least squares fitting the theoretical formula to the Lorentzian curve, which represents diffusivity as a function of mean flow. This method cannot be applied here though because of the heavy computational load required for the global eddying model.

Inspired by Klocker and Abernathey (2013), we estimated the empirical eddy parameters directly from the POP model. The term $C_w(x, y, z)$ is estimated from the

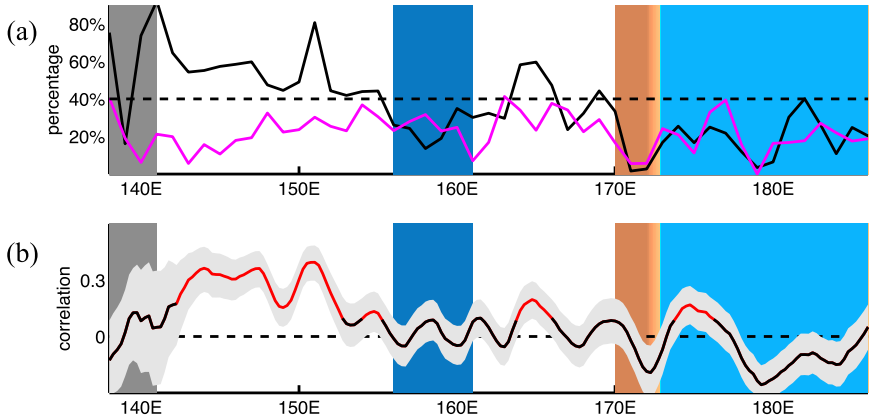

FIG. 12. (a) Percentage of critical layer points that correspond to elevated values of cross-stream mixing length in each latitude–depth cross section (solid lines). Percentage of critical layer points from linear instability analysis (Radon approach) is indicated by the solid magenta (black) line. Black dashed line indicates 40%. The four shaded area from left to right respectively denote the longitude location of four main topographic features shown in Fig. 1: Izu Ridge, Shatsky Rise, Emperor Seamounts, and Hess Rise. (b) The correlation between L_{mix}, from numerical floats, and $L_{\mathrm{mix,theory}}$ at each latitude–depth cross section (solid line). The correlation, which is statistically significantly positive at the 95% confidence level, is indicated by red color on the solid line. Light gray surrounding the solid line indicates 95% uncertainties. Black dashed line indicates zero correlation. The correlation is carried out in areas, where the eddy phase speed estimates are reliable.

Hovmöller diagram method illustrated in Fig. 8, that is, it is equal to $C_{x'}$. Considering that ocean variability has a broad range of wavenumbers and include both vortices and a background field (e.g., McWilliams 1984; Maltrud and Vallis 1991; Polvani et al. 1994; Chelton et al. 2011; Buckingham and Cornillon 2013), we choose k_{eddy} in Eq. (17) to be the centroid of the eddy kinetic energy spectrum, that is,

$$k_{\mathrm{eddy}}(x,y,z) = \frac{\iiint \sqrt{k^2+l^2}\, S_{\mathrm{EKE}}(k,l,\omega)\, dk\, dl\, d\omega}{\iiint S_{\mathrm{EKE}}(k,l,\omega)\, dk\, dl\, d\omega}, \quad (18)$$

where k is the zonal wavenumber, l is the meridional wavenumber, and ω is frequency. The value S_{EKE} is the frequency–wavenumber spectra of eddy kinetic energy in a horizontal patch at depth z, with (x, y) as its center and with a size of 3° × 3°. Following Klocker and Abernathey (2013), we choose L and γ in Eq. (17) to be

$$L(x,y,z) = \frac{2\pi}{k_{\mathrm{eddy}}(x,y,z)} \quad \text{and} \quad \gamma(x,y,z) = \frac{u_{\mathrm{rms}}(x,y,z)}{2\Gamma L(x,y,z)}. \quad (19)$$

3) RESULTS

We estimated the theoretical mixing length $L_{\mathrm{mix,theory}}$ (x, y, z) from Eq. (17), using empirical parameters diagnosed from the POP model. To compare it with the mixing length from floats $[L_{\mathrm{mix}}(x, y, z)]$, we diagnosed the correlation as a function of longitude between the latitude–depth cross sections of $L_{\mathrm{mix,theory}}$ and that of L_{mix} (Fig. 12b). The correlation coefficients are larger than other areas in the longitude range where the KE jet core is intense and away from topography (the red line between the gray and blue area). This statement is also confirmed through comparison of spatial patterns (not shown). The correlation in the topographic regions (shaded area in Fig. 12) is mostly insignificantly different from zero or significantly negative. Therefore, our findings here are consistent with those reported in section 5b: critical layer theory is relevant in the intense jet area away from topography.

The theoretical mixing length formula from Ferrari and Nikurashin (2010) is based on the assumption that the mean flow and eddy phase speeds vary on spatial scales that are larger than the eddy size and that the mean flow has jet parallel structure (Ferrari and Nikurashin 2010; Naveira Garabato et al. 2011). The spatial variation of mean flow and eddy properties due to topography may be one cause of the breakdown of the theory. On the other hand, errors in our estimates of eddy properties near topography may also contribute to the mismatch between L_{mix} and $L_{\mathrm{mix,theory}}$. Our estimates of C_w and k_{eddy} are based on the assumption that the mean flow and eddy properties vary slowly

in space. This assumption likely breaks down near topography.

6. Discussion and summary

Our first goal was to characterize spatially resolved isopycnal eddy mixing rates in the KE region. Isopycnal eddy diffusivities were estimated using a clustering approach that is based on the use of adaptive bins and a large number of numerical pseudo–float tracks. Diffusivities obtained using adaptive bins converge better than those computed using geographic bins. Cross-stream diffusivities, which differ greatly from the eddy velocity magnitude patterns, exhibit small-scale spatial variability, with elevated values in the recirculation gyre region, near topographic features, and in the downstream KE jet, which has greatly weakened.

Our second goal was to examine the vertical structures of cross-stream mixing and assess whether the critical layer theory applies. Besides estimating CLD from linear local baroclinic instability analysis, we also diagnosed CLD from realistic eddy phase speeds using the Radon transform. Considering the breakdown of the linear local baroclinic instability assumption in the intense KE jet area, it is unsurprising that the CLD inferred from realistic eddy phase speeds is a better predictor of elevated mixing in our domain. In the intense jet area away from topography, critical layers occur at depths with large mixing lengths, and the cross-stream mixing length from the theory of Ferrari and Nikurashin (2010) is positively correlated with the float-based mixing length. This indicates a need for detailed process studies focused on the influence of topography on eddies, mixing, and critical layers.

Isopycnal eddy mixing in the KE region and the Southern Ocean have both similarities and differences. First, as in the Southern Ocean (Griesel et al. 2010, 2014), high cross-stream mixing in the KE occurs in some regions with major topographic features, and the jet suppression of cross-stream mixing does not occur everywhere. Second, evidence for the breakdown of critical layer theory has also been identified in the Southern Ocean (Naveira Garabato et al. 2011; Sallée et al. 2011). Third, Abernathey et al. (2010) identified a local maximum of mixing at middepth in the Southern Ocean and attributed it to the critical layer mechanism. However, in the intense KE jet, neither a local maximum of cross-stream mixing nor a critical layer exists.

At least two techniques exist to identify transport barriers, which impede mixing. One way is to estimate diffusivities (e.g., Ferrari and Nikurashin 2010; Abernathey et al. 2013; Griesel et al. 2014). Theories, such as the critical layer theory, have been developed to interpret the diffusivity patterns. An alternative, probably more rigorous, way to detect transport barriers is to use the recently developed geodesic theory from Haller and Beron-Vera (2012). The two techniques are distinct yet related. Diffusivities in this study, in spite of the nonlocal nature of this estimate, denote the averaged mixing rates in a selected finite area in the Eulerian space (i.e., bin) over some time period (e.g., 1 yr). If cross-stream diffusivities are smaller in the time-mean jet than in the surrounding region, then the jet functions as a mixing barrier. In geodesic theory, barriers are identified as instantaneous material lines with locally minimally stretching, which form, move in space with time, and break (Haller and Beron-Vera 2012). Future work will be needed to link these two methods.

Negative eddy diffusivities using Lagrangian methods are, for the first time, identified over the western Izu Ridge and in the downstream KE jet (section 4). Upgradient eddy fluxes occur in the downstream extensions of western boundary currents (see section 1). If the Lagrangian eddy diffusivity estimate converges, the Lagrangian eddy diffusivity is consistent with the Eulerian eddy diffusivity (Davis 1987, 1991; Griesel et al. 2010). Thus, negative Lagrangian diffusivities probably occur in the regions with upgradient eddy fluxes, which correspond to negative Eulerian diffusivities.

One way to further interpret negative diffusivities is to examine float statistics. We examined the autocorrelation, the integrand of Eq. (3):

$$R_{\perp}(\mathbf{x},\tilde{\tau}) = \langle u'_{\perp}(t_0\,|\,\mathbf{x},t_0)u'_{\perp}(t_0+\tilde{\tau}\,|\,\mathbf{x},t_0)\rangle_L\,. \qquad (20)$$

An analytical solution to $R_{\perp}(\mathbf{x}, \tilde{\tau})$ for small-amplitude, single-wavenumber eddies was formulated by Klocker et al. (2012a) [see their Eq. (18)]. The solution predicts first that as $\tilde{\tau}$ increases, $R_{\perp}$ oscillates between positive and negative lobes, while decaying; second, the existence of negative lobes is due to the mismatch between $C_{x'}$ and mean flow magnitude U, that is, the suppression of diffusivity by mean flow; and third, smaller values of $|C_{x'} - U|$ imply a wider lobe in the $\tilde{\tau}$ space. At the Izu Ridge where negative $\kappa_{\perp}$ occurs, $|C_{x'} - U|$ averaged over all the float tracks in the bin decreases as $\tilde{\tau}$ increases due to the flow inhomogeneity. Therefore, the negative lobe following the positive lobe can have a larger area than the positive lobe, and thus $\kappa_{\perp}$ can be negative. Consistent with the above interpretation, the negative diffusivities in these bins are due to the large negative lobes of $R_{\perp}(\mathbf{x}, \tilde{\tau})$. Yet, this mechanism is limited, as the eddy size and other properties can be inhomogeneous too, and the analytical solution is based on several assumptions. Also, the origin of the negative lobe is still under debate (Griesel et al. 2010).

Acknowledgments. R. Chen and J. L. McClean (JLM) were supported by NSF Grants OCE0850463 and OCE0960914. JLM was also supported by U.S. Department of Energy's Office of Science Climate Modeling Programs via a Los Alamos National Laboratory (LANL) subcontract. S. Gille was supported by NASA NNXBAE446 and NSF OCE-1234473. We are grateful to two anonymous reviewers for their helpful comments and to Shafer Smith for sharing the code for the linear instability analysis. We benefited from discussions with Ryan Abernathey, Glenn Flierl, Ayah Lazar, Matthew Mazloff, Andrew Stewart, Lynne Talley, and Andrew Thompson. Many thanks to Mathew Maltrud (LANL) for adapting the online float code to run on the global tripole grid and for explaining the calculation of certain model variables. Elena Yuleava (SIO) is thanked for extracting the POP model output and for discussions about the simulation. Computational resources for the model run were provided by NSF XSEDE Resource Grant TG-OCE100001. Output from this simulation is available at the National Center for Computational Sciences.

APPENDIX

Methodology for the Convergence Test

One way to check whether the diffusivity κ asymptotes to a constant value is to see whether $\kappa(\tau)$ has leveled off as the lead–lag time period τ increases. While the "level-off" can be judged by eye (e.g., Griesel et al. 2010; Klocker et al. 2012a,b; Griesel et al. 2014; LaCasce et al. 2014), we provide a simple quantitative criterion to judge whether $\kappa(\tau)$ asymptotes to a constant in a statistical sense, given the limited number and duration of float data available for assessing κ.

The criterion used to judge the convergence properties of $\kappa(\tau)$ is as follows: Consider positive lags (i.e., $\tau > 0$) in the first instance. Define $\tilde{\sigma}(\tau)$ as two standard errors of $\kappa(\tau)$ using the boot-strap technique in Griesel et al. (2010) and Klocker et al. (2012b). Also define the best-fit straight line for $\kappa(\tau)$ in the range of $\tau \in [\tau_1, \tau_2]$ as

$$\tilde{\kappa}(\tau) = a\tau + b. \tag{A1}$$

If $|a(\tau_2 - \tau_1)|$ is smaller than the minimum value of $2\tilde{\sigma}(\tau)$ in the range of $\tau \in [\tau_1, \tau_2]$, it means that the trend of $\kappa(\tau)$ is statistically insignificant, and thus $\kappa(\tau)$ has leveled off over $\tau_1 - \tau_2$ (asymptotes to a constant) in the statistical sense. Besides the linear fit criterion, if the number of pseudotracks for each bin is less than 100, κ is assumed not to have converged. The convergence criterion for negative lags (i.e., $\tau < 0$) is the same. Figure A1 illustrates the convergence tests: for some bins, diffusivities have converged for both positive and negative τ; while for some others, diffusivities converge for either positive or negative τ or for neither.

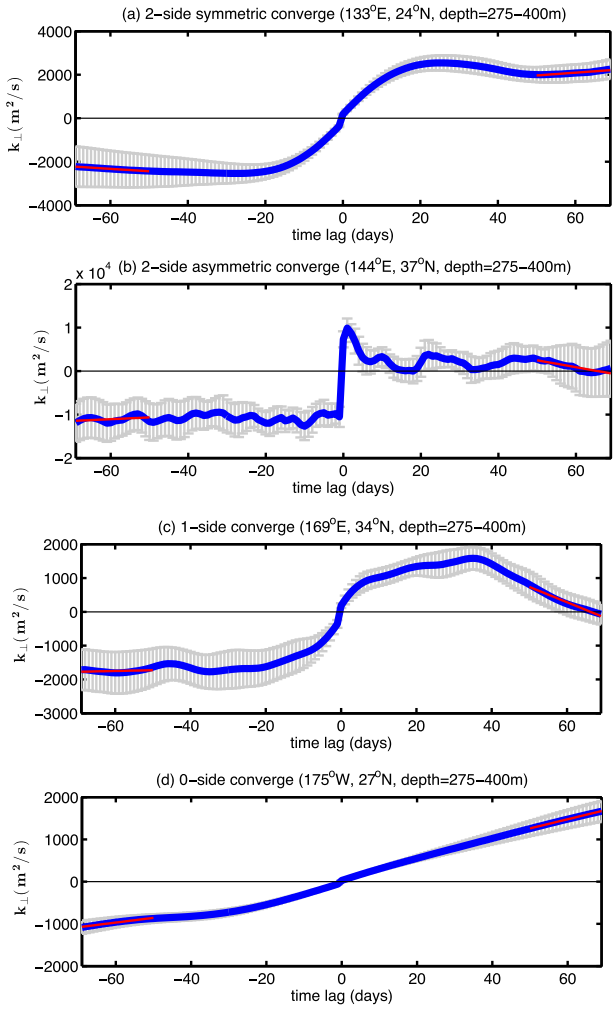

FIG. A1. The term $\kappa_\perp$ for selected adaptive bins (blue lines). Error bars are obtained through boot strapping. We randomly subsample 20 pseudotrajectories each time, and this subsampling is repeated 20 times for each bin. Errors are the two standard deviation of diffusivities estimated from these 20 subsamples. Red lines are the best-fit straight lines for the blue line at 50 ~ 69 day and at −69 ~ −50 day, for the convergence test purpose. (a) The two-side symmetric converge case: cross-stream diffusivity converges on both sides, and the differences between diffusivity estimates on the two sides are smaller than the error bar. (b) The two-side asymmetric converge case: although diffusivity converges on both sides, the differences between diffusivity estimates on the two sides are larger than the error. (c) The case where the diffusivity converges on one side only. (d) The case where the diffusivity converges on neither side.

Our statistical test above is reproducible and robust given the available float trajectories. If the amount of float data increases, the error bar magnitude and the

magnitude of the long-term deterministic trend can be reduced.

In some bins, $\kappa(\tau)$ converges toward different values on the two sides (e.g., Fig. A1b), that is,

$$|\kappa_\infty - \kappa_{-\infty}| > \sqrt{\sigma_\infty^2 + \sigma_{-\infty}^2}, \tag{A2}$$

where $\sigma_{-\infty}$ is the two standard errors of $\kappa_{-\infty}$ from the boot-strap technique and σ_∞ is the two standard errors for κ_∞. In some other bins, $\kappa(\tau)$ converges to the same values on the two sides (e.g., Fig. A1a), that is,

$$|\kappa_\infty - \kappa_{-\infty}| <= \sqrt{\sigma_\infty^2 + \sigma_{-\infty}^2}. \tag{A3}$$

We term the former case "asymmetric convergence" and the latter case "symmetric convergence." Asymmetric convergence has not been identified or emphasized in previous studies, and its causes remain unclear. It could be related to the nonlocal nature of Lagrangian eddy diffusivities, mixing inhomogeneities, or the fluid nonstationarity. If pseudotrajectories entering or leaving the bin are dominated by different dynamical regimes in spatial and temporal space, asymmetric convergence might occur. Another issue is whether this phenomenon is an artifact of high-resolution diffusivity estimates or real physics.

Theory for small-amplitude and single-wavenumber eddies in the constant mean flow predicts that 1) the autocorrelation function for cross-stream diffusivities has both decaying and oscillating parts, 2) a negative lobe tends to follow the positive lobe, and integrating the autocorrelation to the first zero crossing can overestimate diffusivity (Klocker et al. 2012a). The POP model represents a realistic scenario. As reported by Rypina et al. (2012), the autocorrelation functions in some adaptive bins with converged diffusivities have shapes consistent with theory; in some other bins, other shapes are identified. In spite of the various shapes, the magnitude of the autocorrelation function roughly drops to zero or oscillates at small magnitudes at the lead–lag time period when κ has leveled off based on our statistic tests. This is because the diffusivity is the integration of the autocorrelation function.

REFERENCES

Abernathey, R., J. Marshall, M. Mazloff, and E. Shuckburgh, 2010: Enhancement of mesoscale eddy stirring at steering levels in the Southern Ocean. *J. Phys. Oceanogr.,* **40,** 170–184, doi:10.1175/2009JPO4201.1.

——, D. Ferreira, and A. Klocker, 2013: Diagnostics of isopycnal mixing in a circumpolar channel. *Ocean Modell.,* **72,** 1–16, doi:10.1016/j.ocemod.2013.07.004.

Bishop, S. P., D. R. Watts, and K. A. Donohue, 2013: Divergent eddy heat fluxes in the Kuroshio Extension at 144°–148°E. Part I: Mean structure. *J. Phys. Oceanogr.,* **43,** 1533–1550, doi:10.1175/JPO-D-12-0221.1.

Bower, A. S., and H. T. Rossby, 1989: Evidence of cross-frontal exchange processes in the Gulf Stream based on isopycnal RAFOS float data. *J. Phys. Oceanogr.,* **19,** 1177–1190, doi:10.1175/1520-0485(1989)019<1177:EOCFEP>2.0.CO;2.

——, ——, and J. L. Lillibridge, 1985: The Gulf Stream—Barrier or blender? *J. Phys. Oceanogr.,* **15,** 24–32, doi:10.1175/1520-0485(1985)015<0024:TGSOB>2.0.CO;2.

Buckingham, C. E., and P. C. Cornillon, 2013: The contribution of eddies to striations in absolute dynamic topography. *J. Geophys. Res.,* **118,** 448–461, doi:10.1029/2012JC008231.

Cerovecki, I., R. A. Plumb, and W. Heres, 2009: Eddy transport and mixing in a wind- and buoyancy-driven jet on the sphere. *J. Phys. Oceanogr.,* **39,** 1133–1149, doi:10.1175/2008JPO3596.1.

Chelton, D. B., M. G. Schlax, and R. M. Samelson, 2011: Global observations of nonlinear mesoscale eddies. *Prog. Oceanogr.,* **91,** 167–216, doi:10.1016/j.pocean.2011.01.002.

Chen, R., 2013: Energy pathways and structures of oceanic eddies from the ECCO2 state estimate and simplified models. Ph.D. thesis, Massachusetts Institute of Technology and Woods Hole Oceanographic Institution, 206 pp.

——, G. R. Flierl, and C. Wunsch, 2014: A description of local and nonlocal eddy–mean flow interaction in a global eddy-permitting state estimate. *J. Phys. Oceanogr.,* doi:10.1175/JPO-D-14-0009.1, in press.

Danabasoglu, G., and J. Marshall, 2007: Effects of vertical variations of thickness diffusivity in an ocean general circulation model. *Ocean Modell.,* **18,** 122–141, doi:10.1016/j.ocemod.2007.03.006.

Davis, R., 1987: Modelling eddy transport of passive tracers. *J. Mar. Res.,* **45,** 635–666, doi:10.1357/002224087788326803.

——, 1991: Observing the general circulation with floats. *Deep-Sea Res.,* **38A** (Suppl. 1), S531–S571, doi:10.1016/S0198-0149(12)80023-9.

Donohue, K., and Coauthors, 2008: Program studies of the Kuroshio Extension. *Eos, Trans. Amer. Geophys. Union,* **89,** 161–162, doi:10.1029/2008EO170002.

Döös, K., and D. Webb, 1994: The Deacon cell and other meridional cells of the Southern Ocean. *J. Phys. Oceanogr.,* **24,** 429–442, doi:10.1175/1520-0485(1994)024<0429:TDCATO>2.0.CO;2.

Drijfhout, S. S., 2005: What sets the surface eddy mass flux in the Southern Ocean? *J. Phys. Oceanogr.,* **35,** 2152–2166, doi:10.1175/JPO2776.1.

Dukowicz, J. K., and R. D. Smith, 1994: Implicit free-surface method for the Bryan-Cox-Semtner ocean model. *J. Geophys. Res.,* **99,** 7991–8014, doi:10.1029/93JC03455.

Eden, C., R. J. Greatbatch, and J. Willebrand, 2007: A diagnosis of thickness fluxes in an eddy-resolving model. *J. Phys. Oceanogr.,* **37,** 727–742, doi:10.1175/JPO2987.1.

Ferrari, R., and C. Wunsch, 2009: Ocean circulation kinetic energy: Reservoirs, sources, and sinks. *Annu. Rev. Fluid Mech.,* **41,** 253–282, doi:10.1146/annurev.fluid.40.111406.102139.

——, and M. Nikurashin, 2010: Suppression of eddy diffusivity across jets in the Southern Ocean. *J. Phys. Oceanogr.,* **40,** 1501–1519, doi:10.1175/2010JPO4278.1.

Gent, P. R., and J. C. McWilliams, 1990: Isopycnal mixing in ocean circulation models. *J. Phys. Oceanogr.,* **20,** 150–155, doi:10.1175/1520-0485(1990)020<0150:IMIOCM>2.0.CO;2.

Green, J. S. A., 1970: Transport properties of the large-scale eddies and the general circulation of the atmosphere. *Quart. J. Roy. Meteor. Soc.,* **96,** 157–185, doi:10.1002/qj.49709640802.

Greene, A. D., G. G. Sutyrin, and D. R. Watts, 2009: Deep cyclogenesis by synoptic eddies interacting with a seamount. *J. Mar. Res.,* **67,** 305–322, doi:10.1357/002224009789954775.

——, D. R. Watts, G. G. Sutyrin, and H. Sasaki, 2012: Evidence of vertical coupling between the Kuroshio Extension and topographically controlled deep eddies. *J. Mar. Res.,* **70,** 719–747, doi:10.1357/002224012806290723.

Griesel, A., S. T. Gille, J. Sprintall, J. L. McClean, J. H. LaCasce, and M. E. Maltrud, 2010: Isopycnal diffusivities in the Antarctic Circumpolar Current inferred from Lagrangian floats in an eddying model. *J. Geophys. Res.,* **115,** C06006, doi:10.1029/2009JC005821.

——, J. L. McClean, S. T. Gille, J. Sprintall, and C. Eden, 2014: Eulerian and Lagrangian isopycnal eddy diffusivities in the Southern Ocean of an eddying model. *J. Phys. Oceanogr.,* **44,** 644–661, doi:10.1175/JPO-D-13-039.1.

Haller, G., and F. J. Beron-Vera, 2012: Geodesic theory of transport barriers in two-dimensional flows. *Physica D,* **241,** 1680–1702, doi:10.1016/j.physd.2012.06.012.

Howe, P., K. A. Donohue, and D. R. Watts, 2009: Stream-coordinate structure and variability of the Kuroshio Extension. *Deep-Sea Res. I,* **56,** 1093–1116, doi:10.1016/j.dsr.2009.03.007.

Hurlburt, H. E., and E. J. Metzger, 1998: Bifurcation of the Kuroshio Extension at the Shatsky Rise. *J. Geophys. Res.,* **103,** 7549–7566, doi:10.1029/97JC02723.

Jayne, S. R., and Coauthors, 2009: The Kuroshio Extension and its recirculation gyres. *Deep-Sea Res. I,* **56,** 2088–2099, doi:10.1016/j.dsr.2009.08.006.

Killworth, P. D., 1997: On the parameterization of eddy transfer. Part I. Theory. *J. Mar. Res.,* **55,** 1171–1197, doi:10.1357/0022240973224102.

Klocker, A., and R. Abernathey, 2013: Global patterns of mesoscale eddy properties and diffusivities. *J. Phys. Oceanogr.,* **44,** 1030–1046, doi:10.1175/JPO-D-13-0159.1.

——, R. Ferrari, and J. H. LaCasce, 2012a: Estimating suppression of eddy mixing by mean flows. *J. Phys. Oceanogr.,* **42,** 1566–1576, doi:10.1175/JPO-D-11-0205.1.

——, ——, ——, and S. Merrifield, 2012b: Reconciling float-based and tracer-based estimates of eddy diffusivities. *J. Mar. Res.,* **70,** 569–602, doi:10.1357/002224012805262743.

Koszalka, I. M., and J. H. LaCasce, 2010: Lagrangian analysis by clustering. *Ocean Dyn.,* **60,** 957–972, doi:10.1007/s10236-010-0306-2.

——, ——, M. Andersson, K. A. Orvik, and C. Mauritzen, 2011: Surface circulation in the Nordic Seas from clustered drifters. *Deep-Sea Res. I,* **58,** 468–485, doi:10.1016/j.dsr.2011.01.007.

Kouketsu, S., and I. Yasuda, 2008: Unstable frontal waves along the Kuroshio Extension with low-potential vorticity intermediate Oyashio water. *J. Phys. Oceanogr.,* **38,** 2308–2321, doi:10.1175/2008JPO3814.1.

LaCasce, J. H., R. Ferrari, J. Marshall, R. Tulloch, D. Balwada, and K. Speer, 2014: Float-derived isopycnal diffusivities in the DIMES experiment. *J. Phys. Oceanogr.,* **44,** 764–780, doi:10.1175/JPO-D-13-0175.1.

Large, W. G., and S. G. Yeager, 2009: The global climatology of an interannually varying air–sea flux data set. *Climate Dyn.,* **33,** 341–364, doi:10.1007/s00382-008-0441-3.

——, J. C. McWilliams, and S. C. Doney, 1994: Oceanic vertical mixing: A review and a model with nonlocal boundary layer parameterization. *Rev. Geophys.,* **32,** 363–403, doi:10.1029/94RG01872.

Lebedev, K. V., M. Yaremchuk, H. Mitsudera, I. Nakano, and G. Yuan, 2003: Monitoring the Kuroshio Extension with dynamically constrained synthesis of the acoustic tomography, satellite altimeter and in situ data. *J. Oceanogr.,* **59,** 751–763, doi:10.1023/B:JOCE.0000009568.06949.c5.

Lozier, M. S., and D. Bercovici, 1992: Particle exchange in an unstable jet. *J. Phys. Oceanogr.,* **22,** 1506–1516, doi:10.1175/1520-0485(1992)022<1506:PEIAUJ>2.0.CO;2.

Maltrud, M. E., and G. K. Vallis, 1991: Energy spectra and coherent structures in forced two-dimensional and beta-plane turbulence. *J. Fluid Mech.,* **228,** 321–342, doi:10.1017/S0022112091002720.

——, R. D. Smith, A. J. Semtner, and A. J. Malone, 1998: Global eddy-resolving ocean simulations driven by 1985–1995 atmospheric winds. *J. Geophys. Res.,* **103,** 30 825–30 853, doi:10.1029/1998JC900013.

——, F. O. Bryan, and S. Peacock, 2010: Boundary impulse response functions in a century-long eddying global ocean simulation. *Environ. Fluid Mech.,* **10,** 275–295, doi:10.1007/s10652-009-9154-3.

Marshall, J., and G. Shutts, 1981: A note on rotational and divergent eddy fluxes. *J. Phys. Oceanogr.,* **11,** 1677–1680, doi:10.1175/1520-0485(1981)011<1677:ANORAD>2.0.CO;2.

——, E. Shuckburgh, H. Jones, and C. Hill, 2006: Estimates and implications of surface eddy diffusivity in the Southern Ocean derived from tracer transport. *J. Phys. Oceanogr.,* **36,** 1806–1821, doi:10.1175/JPO2949.1.

Maximenko, N. A., B. Bang, and H. Sasaki, 2005: Observational evidence of alternating zonal jets in the world ocean. *Geophys. Res. Lett.,* **32,** L12607, doi:10.1029/2005GL022728.

——, O. V. Melnichenko, P. P. Niiler, and H. Sasaki, 2008: Stationary mesoscale jet-like features in the ocean. *Geophys. Res. Lett.,* **35,** L08603, doi:10.1029/2008GL033267.

McClean, J. L., P. M. Poulain, J. W. Pelton, and M. E. Maltrud, 2002: Eulerian and Lagrangian statistics from surface drifters and a high-resolution POP simulation in the North Atlantic. *J. Phys. Oceanogr.,* **32,** 2472–2491, doi:10.1175/1520-0485-32.9.2472.

McWilliams, J. C., 1984: The emergence of isolated coherent vortices in turbulent flow. *J. Fluid Mech.,* **146,** 21–43, doi:10.1017/S0022112084001750.

Morrow, R., R. Coleman, J. Church, and D. Chelton, 1994: Surface eddy momentum flux and velocity variances in the Southern Ocean from Geosat altimetry. *J. Phys. Oceanogr.,* **24,** 2050–2071, doi:10.1175/1520-0485(1994)024<2050:SEMFAV>2.0.CO;2.

Naveira Garabato, A. C., R. Ferrari, and K. L. Polzin, 2011: Eddy stirring in the Southern Ocean. *J. Geophys. Res.,* **116,** C09019, doi:10.1029/2010JC006818.

Oka, E., and B. Qiu, 2012: Progress of North Pacific mode water research in the past decade. *J. Oceanogr.,* **68,** 5–20, doi:10.1007/s10872-011-0032-5.

Owens, W. B., 1984: A synoptic and statistical description of the Gulf Stream and subtropical gyre using SOFAR floats. *J. Phys. Oceanogr.,* **14,** 104–113, doi:10.1175/1520-0485(1984)014<0104:ASASDO>2.0.CO;2.

Pacanowski, R. C., and A. Gnanadesikan, 1998: Transient response in a z-level ocean model that resolves topography with partial cells. *Mon. Wea. Rev.,* **126,** 3248–3270, doi:10.1175/1520-0493(1998)126<3248:TRIAZL>2.0.CO;2.

Polvani, L. M., J. C. McWilliams, M. A. Spall, and R. Ford, 1994: The coherent structures of shallow-water turbulence:

Deformation-radius effects, cyclone/anticyclone asymmetry and gravity-wave generation. *Chaos,* **4,** 177–186, doi:10.1063/1.166002.

Qiu, B., 1995: Variability and energetics of the Kuroshio Extension and its recirculation gyre from the first two-year TOPEX data. *J. Phys. Oceanogr.,* **25,** 1827–1842, doi:10.1175/1520-0485(1995)025<1827:VAEOTK>2.0.CO;2.

——, and S. Chen, 2011: Effect of decadal Kuroshio Extension jet and eddy variability on the modification of North Pacific Intermediate Water. *J. Phys. Oceanogr.,* **41,** 503–515, doi:10.1175/2010JPO4575.1.

——, ——, and P. Hacker, 2007: Effect of mesoscale eddies on Subtropical Mode Water variability from the Kuroshio Extension System Study (KESS). *J. Phys. Oceanogr.,* **37,** 982–1000, doi:10.1175/JPO3097.1.

Redi, M. H., 1982: Oceanic isopycnal mixing by coordinate rotation. *J. Phys. Oceanogr.,* **12,** 1154–1158, doi:10.1175/1520-0485(1982)012<1154:OIMBCR>2.0.CO;2.

Roberts, M. J., and D. P. Marshall, 2000: On the validity of downgradient eddy closures in ocean models. *J. Geophys. Res.,* **105,** 28 613–28 627, doi:10.1029/1999JC000041.

Rypina, I. I., I. Kamenkovich, P. Berloff, and L. Pratt, 2012: Eddy-induced particle dispersion in the near-surface Atlantic. *J. Phys. Oceanogr.,* **42,** 2206–2228, doi:10.1175/JPO-D-11-0191.1.

Sallée, J. B., K. Speer, and S. R. Rintoul, 2011: Mean-flow and topographic control on surface eddy-mixing in the Southern Ocean. *J. Mar. Res.,* **69,** 753–777, doi:10.1357/002224011799849408.

Shuckburgh, E., H. Jones, J. Marshall, and C. Hill, 2009: Understanding the regional variability of eddy diffusivity in the Pacific sector of the Southern Ocean. *J. Phys. Oceanogr.,* **39,** 2011–2023, doi:10.1175/2009JPO4115.1.

Smith, K. S., 2007: The geography of linear baroclinic instability in Earth's oceans. *J. Mar. Res.,* **65,** 655–683, doi:10.1357/002224007783649484.

——, and J. Marshall, 2009: Evidence for enhanced eddy mixing at middepth in the Southern Ocean. *J. Phys. Oceanogr.,* **39,** 50–69, doi:10.1175/2008JPO3880.1.

Talley, L. D., Y. Nagata, M. Fujimura, T. Iwao, T. Kono, D. Inagake, M. Hirai, and K. Okuda, 1995: North Pacific Intermediate Water in the Kuroshio/Oyashio mixed water region. *J. Phys. Oceanogr.,* **25,** 475–501, doi:10.1175/1520-0485(1995)025<0475:NPIWIT>2.0.CO;2.

Taylor, G. I., 1915: Eddy motion in the atmosphere. *Philos. Trans. Roy. Soc. London,* **A215,** 1–26, doi:10.1098/rsta.1915.0001.

——, 1921: Diffusion by continuous movements. *Proc. London Math. Soc.,* **20,** 196–211, doi:10.1112/plms/s2-20.1.196.

Thompson, A. F., 2008: The atmospheric ocean: Eddies and jets in the Antarctic Circumpolar Current. *Philos. Trans. Roy. Soc. London,* **366,** 4529–4541, doi:10.1098/rsta.2008.0196.

——, 2010: Jet formation and evolution in baroclinic turbulence with simple topography. *J. Phys. Oceanogr.,* **40,** 257–278, doi:10.1175/2009JPO4218.1.

——, and J. B. Sallée, 2012: Jets and topography: Jet transitions and the impact on transport in the Antarctic Circumpolar Current. *J. Phys. Oceanogr.,* **42,** 956–972, doi:10.1175/JPO-D-11-0135.1.

Tracey, K. L., D. R. Watts, K. A. Donohue, and H. Ichikawa, 2012: Propagation of Kuroshio Extension meanders between 143° and 149°E. *J. Phys. Oceanogr.,* **42,** 581–601, doi:10.1175/JPO-D-11-0138.1.

Visbeck, M., J. Marshall, T. Haine, and M. Spall, 1997: Specification of eddy transfer coefficients in coarse-resolution ocean circulation models. *J. Phys. Oceanogr.,* **27,** 381–402, doi:10.1175/1520-0485(1997)027<0381:SOETCI>2.0.CO;2.

Vollmer, L., and C. Eden, 2013: A global map of mesoscale eddy diffusivities based on linear stability analysis. *Ocean Modell.,* **72,** 198–209, doi:10.1016/j.ocemod.2013.09.006.

Waterman, S. N., and S. R. Jayne, 2011: Eddy-mean flow interaction in the along-stream development of a western boundary current jet: An idealized model study. *J. Phys. Oceanogr.,* **41,** 682–707, doi:10.1175/2010JPO4477.1.

——, and B. J. Hoskins, 2013: Eddy shape, orientation, propagation, and mean flow feedback in western boundary current jets. *J. Phys. Oceanogr.,* **43,** 1666–1690, doi:10.1175/JPO-D-12-0152.1.

——, N. G. Hogg, and S. R. Jayne, 2011: Eddy-mean flow interaction in the Kuroshio Extension region. *J. Phys. Oceanogr.,* **41,** 1182–1208, doi:10.1175/2010JPO4564.1.

Wortham, C. J., 2013: A multi-dimensional spectral description of ocean variability with applications. Ph.D. thesis, Massachusetts Institute of Technology and Woods Hole Oceanographic Institution, 184 pp.

Wunsch, C., 1998: The work done by the wind on the oceanic general circulation. *J. Phys. Oceanogr.,* **28,** 2332–2340, doi:10.1175/1520-0485(1998)028<2332:TWDBTW>2.0.CO;2.

——, 2010: Toward a midlatitude ocean frequency–wavenumber spectral density and trend determination. *J. Phys. Oceanogr.,* **40,** 2264–2281, doi:10.1175/2010JPO4376.1.

Yuan, G. C., L. J. Pratt, and C. K. R. T. Jones, 2004: Cross-jet Lagrangian transport and mixing in a 2½-layer model. *J. Phys. Oceanogr.,* **34,** 1991–2005, doi:10.1175/1520-0485(2004)034<1991:CLTAMI>2.0.CO;2.

Zhurbas, V., and I. S. Oh, 2003: Lateral diffusivity and Lagrangian scales in the Pacific Ocean as derived from drifter data. *J. Geophys. Res.,* **108,** 3141, doi:10.1029/2002JC001596.